Application and validation of incrementally complex models for wind turbine aerodynamics, isolated wind turbine in uniform inflow conditions

Chris Gundling[1], Jay Sitaraman[1], Beatrice Roget[1] and Pierangelo Masarati[2]

[1] Department of Mechanical Engineering, Wind Energy Research Center, University of Wyoming, Laramie, WY, USA

Received 15 May 2013; Revised 11 June 2014; Accepted 20 July 2014

1. INTRODUCTION

The growing size and investment cost of wind turbines have created an equally growing demand for more reliable design methods. In order to improve the cost competitiveness of wind energy when compared with other forms of energy production, significant efficiency improvements in individual turbine design, as well as wind farm design, must be realized. In the ideal case, improved numerical analysis methods, site testing, and wind tunnel testing can be used together to better understand the fundamental fluid dynamics principles involved in wind turbine aerodynamics. Unfortunately, there are many circumstances, especially when studying wind turbine wakes, where the experimental data that includes detailed geometry of the turbine blades is limited. In the absence of extensive measurement data sets, it is valuable to have a suite of various modeling methods, as it provides the ability to cross-compare data between the models that might not be available from the experiment. A suite that includes models of incremental complexity also provides varying simulation times depending on the solution detail that is required. We suggest that this type of multi-model strategy can be applied for industrial circumstances where demand is placed on faster modeling times and efficient use of computational resources.

Depending on the level of detail needed and time requirements for simulations, a user would have the option of selecting the appropriate method knowing a priori the strengths of each model.

Previous articles by Crespo *et al*.,[1] Vermeer *et al*.,[2] and Troldborg *et al*.[3] have discussed the most influential work in this field and have introduced the issues being faced by the wind turbine performance and wake modeling community. There are significant current efforts to improve the understanding of the near and far wake with increasingly complex vortex, Reynolds-averaged Navier–Stokes (RANS), large eddy simulation (LES), and detached eddy simulation (DES)-based methods that incorporate actuator line/disc/surface and full rotor representations of the turbines.

The objective of this research is to develop a platform for a multi-fidelity turbine aerodynamic performance and wake prediction tool. Three models will be tested side by side in increasingly complex wind farm situations to give a complete picture of the capabilities of each method. In this article, we focus on an isolated wind turbine in uniform inflow conditions (both axial and yawed). The objectives of this article are as follows:

1. The National Renewable Energy Laboratory (NREL) Phase VI experimental test case is used to validate the single turbine performance and loads prediction in axial and yawed inflow for each of the incrementally complex models. An aeroelastic analysis is performed at varying yaw angles by coupling the models with the multibody solver (MBDyn). Characterizing the level of detail that each model captures at the turbine will also help to explain the differences in the downstream wake. The analysis models in increasing order of complexity are:
   (a) Free-vortex wake analysis using a blade element model (*UWAKE*)
   (b) RANS and LES with an actuator disc using a blade element model (*FLOWYO*)
   (c) Overset grid based RANS and DES using full rotor model (*HELIOS*)
2. The wind speed deficits in the wake generated by the NREL Phase VI turbine in uniform inflow conditions are also analyzed. In particular, the differences in the wake details between the lower complexity models (FLOWYO/UWAKE) and HELIOS predictions are quantified. Modeling the single wake correctly is the first step to designing an accurate and flexible wind farm model.

The NREL Phase VI data were chosen for the first validation step due in part to the large number of models that have been used to simulate the experimental results. Because the NREL Phase VI experimental data were published, there have been many RANS computational fluid dynamics (CFD)[4–11] and vortex methods[12–14] applied to the Phase VI rotor with varying outcomes.

In the second part of the results, the focus is shifted to using each of the three methods to simulate the wake velocities of the Phase VI turbine. The NREL Phase VI experiment was not focused on wake measurements, so these initial wake simulations are only cross-compared between the methods. Before these models are applied to more complex wake scenarios, it was deemed a logical first step to test a single turbine wake in uniform inflow. The NREL Phase VI data are ideal for wake simulations using a variety of models due to the availability of specific turbine blade information such as the twist, chord, airfoil distributions, and blade geometry. This makes it possible to create both a full rotor model and also to use the two-dimensional (2-D) airfoil data for the blade element-based methods.

2. VALIDATION DATA

2.1. National Renewable Energy Laboratory Phase VI

One of the most significant developments in wind research over the past 10 years was provided by the NREL full-scale wind tunnel experiment, which conducted tests on an instrumented wind turbine in the NASA-Ames wind tunnel.[15] The NREL Phase VI rotor geometry, aerodynamic, and structural properties have been well-documented in the literature,[15–17] so only brief details are given.

For the upwind axial and yawed cases, the wind speed was varied from 5 to 25 meters per second ($m\ s^{-1}$), and the turbine rotated at 72 rotations per minute. The rotor radius (R) was 5.029 meters (m), and the tip pitch was 3°. The rotor was attached to a free-standing cylindrical tower with a height of 12.2 m, designed to align the rotor hub with the wind tunnel centerline. There was no fixed tripping on the blade and free transition was allowed. The Phase VI rotor is a stall-regulated turbine with the power generated being limited due to rotor stall.

3. METHODOLOGY

3.1. *UWAKE* Free-vortex wake with a blade element model

The in-house free-vortex wake approach UWAKE[18] uses a Lagrangian formulation of the vorticity-transport equation to model the time evolution of vorticity fields. Considering the dominant structures in the wind turbine flow field to be the

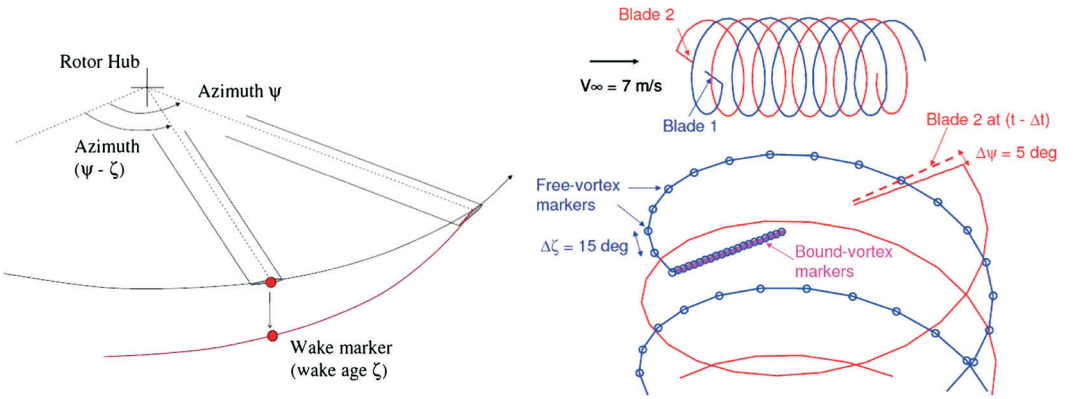

(a) Representaion of tip wake filament and wake marker **(b)** Converged free-vortex wake for Phase VI turbine at 7 $m\ s^{-1}$

Figure 1. National Renewable Energy Laboratory Phase VI free-vortex wake tip visualization

tip and root vortices, the present analysis considers a single tip and root vortex for each wind turbine blade, released from the blade tip and root, respectively. The vortex elements are assumed to convect with the fluid particles. The governing vorticity transport equation can be expressed in Lagrangian form as

$$\frac{d\vec{r}(\psi,\zeta)}{dt} = \vec{V}(\vec{r}(\psi,\zeta)), \tag{1}$$

where $\vec{r}(\psi,\zeta)$ defines the position vector of a wake marker, located on a vortex filament that is trailed from a turbine blade located at an azimuth ψ and wake-age ζ. This wake marker was first created when the blade was located at an azimuth $(\psi - \zeta)$, as represented in Figure 1(a). Figure 1(b) also shows an example of the free wake generated from the blade tip for the NREL Phase VI two-bladed turbine.

The vorticity transport equation can then be written in partial differential form as

$$\frac{\partial\vec{r}(\psi,\zeta)}{\partial\psi} + \frac{\partial\vec{r}(\psi,\zeta)}{\partial\zeta} = \frac{1}{\Omega}\vec{V}(\vec{r}(\psi,\zeta)), \tag{2}$$

where the turbine's rotational speed is given by Ω. The right hand side velocity, $\vec{V}(\vec{r}(\psi,\zeta))$, accounts for the instantaneous velocity field encountered by a marker on a vortex filament in the rotor wake. This includes the free-stream velocity, the induced velocities due to the vortex filaments present in the wake, and the induced contributions of the bound circulation representing the lifting turbine blades. This equation is discretized into a set of finite difference equations that can then be numerically integrated. The time marching algorithm is a 2nd-order backward predictor corrector algorithm and is based on the work by Bhagwat.[19] The velocity term in the vorticity transport equation is computed from the Biot–Savart law:

$$\vec{V}(\vec{r}) = \frac{\Gamma}{4\pi}\frac{h^2}{\sqrt{h^2 + r_c^2}}\int\frac{d\vec{l}\times d\vec{r}}{|\vec{r}|^3}, \tag{3}$$

where $\vec{V}(\vec{r})$ is the velocity induced at a point P located at $\vec{r}$ relative to the vortex element $d\vec{l}$. The integral is evaluated over the entire length of the vortex filament. Γ is the total strength of the filament, and $d\vec{l}$ is an elemental unit vector along the vortex filament. The free-vortex method does not model a shed vortex sheet from the blade. The vortex sheets trailed by the blades are assumed to roll up into tip and root vortices a short distance behind the blade, which has been verified in a number of experiments and CFD computations.[20,21] The strengths of both the root and tip vortices are taken to be equal to the maximum bound circulation along the outboard half of the blade. It is assumed that all the vorticity outboard of maximum bound circulation rolls up into the tip vortex, and all the vorticity inboard of the maximum bound circulation rolls up into the root vortex. Note that the root circulation has the opposite sign of the tip circulation to conform with Helmholtz's second law. The tip and root vortex core radius is noted r_c, and h is the perpendicular distance of the evaluation point from the influencing vortex element. Viscous diffusion is modeled by the growth of the core radius given by Squire[22]

$$r_c(\zeta) = \sqrt{r_0^2 + \frac{4\alpha\delta\nu\zeta}{\Omega}}, \tag{4}$$

where, $\alpha = 1.25643$, is an empirical factor, δ is the apparent viscosity coefficient, ν is the kinematic viscosity, r_0 is the initial vortex core radius, and Ω is the rotational speed of the rotor. The δ parameter is determined by the vortex Reynolds number Re_ν, which is dependent on the tip and root vortex circulation strength Γ_ν,

$$Re_\nu = \frac{\Gamma_\nu}{\nu}. \tag{5}$$

δ is then formulated as,

$$\delta = 1 + a_1 Re_\nu. \tag{6}$$

The empirical factor a_1 has been determined in the past by Ramasamy,[23] and the value of δ should range between 10^1 and 10^5 depending on the scale of the turbine in question.

An appropriate aerodynamic model for the blades needs to be coupled with a free-vortex wake model to predict both the wake evolution as well as the blade loading. UWAKE utilizes a blade element model for the aerodynamic modeling, with aerodynamic coefficients interpolated from tabulated 2D airfoil data. The details of the implemented model can be found in Leishman's book[24] on helicopter aerodynamics. In addition, the Du-Selig[25] stall-delay model is included to account for the aerodynamics at separated flow conditions.

3.1.1. Parameter sensitivity study.

A sensitivity study at $7m\ s^{-1}$ for the downstream wind velocities at 5 R, 10 R, 15 R, and 20 R and power of the NREL turbine was performed to better understand the influence of the critical parameters utilized in the UWAKE method. Figure 2 shows the resulting wind velocities for the variation of four different parameters. Of the four parameters that are varied in

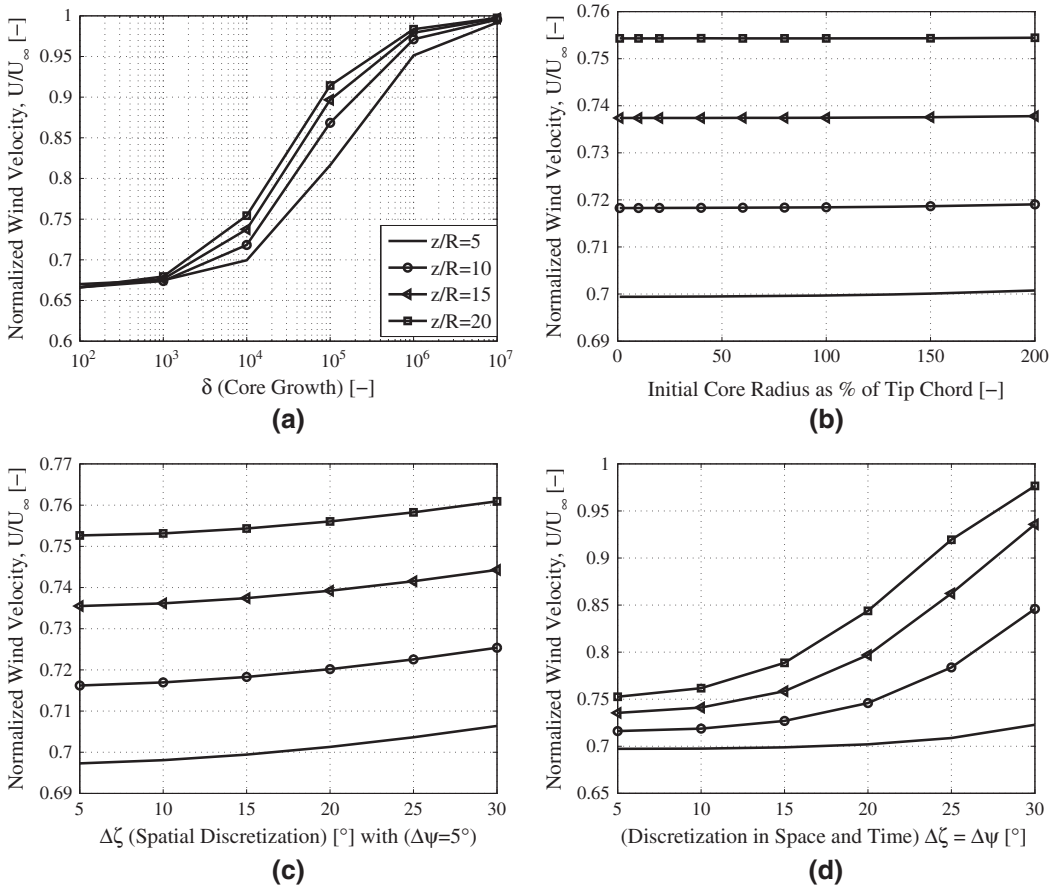

Figure 2. UWAKE wake wind deficit sensitivity study at $7m\ s^{-1}$, for variation of: (a) apparent viscosity coefficient, δ, (b) tip and root vortex initial core radius as % of tip-chord r_0, (c) spatial discretization $\Delta\zeta$, and (d) space and time discretization $\Delta\zeta = \Delta\psi$.

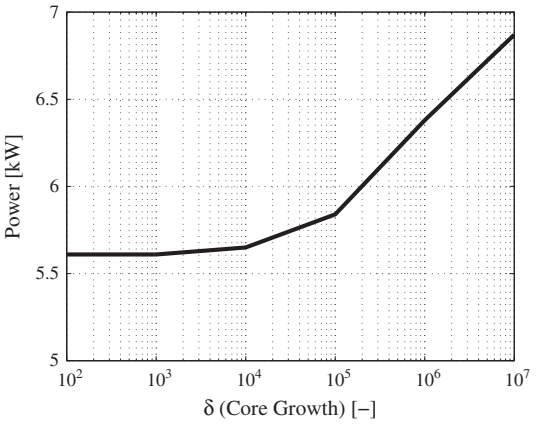

Figure 3. UWAKE power sensitivity at $7m\ s^{-1}$, for variation of apparent viscosity coefficient, δ.

the study, the apparent viscosity or the vortex core growth rate parameter, δ, had the greatest effect on the wake velocities. This is comparable with the eddy-viscosity dependence in RANS CFD turbulence models. As the δ parameter is increased, the diffusion of the wake increases, and the wake velocity deficit recovers at a faster rate. From this study, it is expected that the calculated value of δ at $7\ m\ s^{-1}$ should be near 10^3, which is consistent with the value produced using equations (5) and (6).

For the discretization parameters, varying the spatial discretization, $\Delta\zeta$, alone while the time discretization, $\Delta\psi$, is kept fixed at a small value of 5° does not significantly alter converged velocity values, as shown in Figure 2(c). This justifies using a larger value for the spatial discretization to decrease the computation time without unacceptable loss in accuracy. It should be noted that as each individual parameter is varied, the other variables are held constant at values of $\delta = 10^4$, $\Delta\zeta = 15^\circ$, and $\Delta\psi = 5^\circ$. From Figure 2(d), it can be noted that the combination of spatial and time discretization has a larger effect on the wake velocities, so the time discretization is kept at 5° for all simulations. The impact of the number of points modeled along each blade and the number of wake revolutions modeled were also studied and were found to have a negligible effect on the wake velocities above certain minimum values.

Further interpretation of the effect of the δ parameter can be gathered by examining the power sensitivity of the turbine for increasing values of δ, as shown in Figure 3. The Phase VI turbine produces approximately 6 kWs of power at a wind speed of $7\ m\ s^{-1}$. The turbine power increases with increasing δ because the added δ causes an increase in size of the vortex core, leading to less induced velocity at the rotor. The model solution will significantly diverge from theory and the experimental values if δ is chosen to be too large.

3.1.2. Computational setup.

On the basis of the sensitivity study, the discretization steps used in UWAKE were set to $\Delta\psi = 5^\circ$ (time discretization) and $\Delta\zeta = 15^\circ$ (spatial discretization). The aerodynamic loading was computed at 20 uniformly spaced points along each blade. Two-dimensional wind tunnel data for the S809 airfoil from Ohio State University[26] was used for the NREL turbine, which was taken at a Reynolds number of 1×10^6. Along with the general blade element model theory, a stall delay model by Du-Selig[25] was also applied. A stall delay model is needed because of the elevated lift that is produced from the increased radial flow from the separated areas of the blade. This increased radial flow can act to alleviate adverse pressure gradients. The Du-Selig model was modified on the basis of the work of Breton *et al.*[27] in which several stall delay models are analyzed for the NREL Phase VI turbine.

It should be noted that the convergence of values such as turbine power and wake velocities in UWAKE depend on both the wake-age modeled with spatial markers, and the number of wake revolutions simulated temporally. A general practice adopted with UWAKE was to first determine the wake-age that is needed to be modeled to achieve convergence. The wake evolution can then be simulated for several more revolutions temporally to show convergence in time at each wake marker.

For the performance prediction, it was observed that modeling the vortex wake up to five rotor revolutions of wake-age (480 wake markers per blade) is sufficient to obtain converged results. The free-wake was simulated (starting from zero initial conditions) for 10 rotor revolutions, corresponding to wall-clock execution time of about 10 s. All cases were run on a single Intel Xeon 2.67 GH processor.

For the single turbine far wake velocity predictions, the wake-age was modeled up to 50 rotor revolutions (4800 wake markers per blade), in order to capture the velocity field up to 20 R behind the turbine. The free-wake was simulated for 60 rotor revolutions, corresponding to an execution time of 100 min on the same Intel CPU mentioned earlier. UWAKE is

also capable of running in parallel, but the time savings are most beneficial when modeling large arrays of turbines where millions of wake markers are used. The induced velocity at each individual wake marker is dependent on every other wake marker, which means that the execution time in the current implementation varies with the square of the number of vortex filaments used to discretize the wake. For the performance calculations with 480 wake markers per blade compared with the far wake calculations with 4800 wake markers per blade, though there are only 10× as many wake markers, this creates 100× the number of calculations per time step. This explains the increase in simulation time from 10 s to 100 min for these two cases.

In the results shown for UWAKE, the δ parameter was calculated for each wind speed using equations (5) and (6). This method produced a $\delta = 1100$ at 5 $m\ s^{-1}$ and $\delta = 700$ at 10 $m\ s^{-1}$. The tip chord for the NREL turbine is 0.358 m, the chord at the root is 0.737 m, and the thickness of the blade is 20.95% of the chord at each location. Using this information, the initial core radius for the tip and root were chosen as the thickness of the blade at their respective location. This gave an initial tip core radius of 0.075 m and an initial root core radius of 0.15 m.

3.2. *FLOWYO* actuator disc model

FLOWYO[18] is a finite volume method that solves the Navier Stokes (N–S) equations in their conservative form for compressible flows. Spatial discretization is carried out using a third-order upwind scheme for inviscid terms and a fourth-order central discretization for viscous terms. Temporal discretization is accomplished using a second-order backward differential formula (BDF2) with variable time stepping. FLOWYO is capable of both RANS and LES calculations. For RANS, the Spalart-Allmaras (S–A) turbulence model[28] was used, where as the Smagorinsky sub-grid scale (SGS) turbulence model[29] was used for all LES calculations. The wind turbine is modeled as an actuator disc, which involves inclusion of appropriate source terms in the momentum and energy components of the N–S equations. This approach has been quite popular as a mid-complexity analysis scheme for wind turbines.[30–33] The aerodynamic loading on the wind turbine blade is computed using a simple blade element model with the inflow angle computed using the velocities from CFD calculations. In essence, the coupling between the blade element model and the CFD is as follows; the blade element model provides the aerodynamic loading that is used to compute the source terms in the N–S equations at grid locations corresponding to the disc location. The velocity field obtained from the solution of the N–S equations (with the additional source terms) is in turn used to compute the aerodynamic loading using the blade element model. This solution scheme is iterated until both the aerodynamic loading and the flow field converge and become consistent.

To further describe the source term implementation, the product of the blade element calculations are the normal force (F_z) and tangential force (F_x) at every 2D ($radial(r), azimuthal(\theta)$) location on the cylindrical disc. F_z and F_x are calculated using the following equations

$$F_z = L\cos(\phi) + D\sin(\phi) \quad \text{and} \quad F_x = L\sin(\phi) - D\cos(\phi), \tag{7}$$

where L is the lift given by $L = 1/2\rho U^2 c C_l$, D is the drag, $D = 1/2\rho U^2 c C_d$, and ϕ is the inflow angle. For the lift and drag equations, ρ is the density, c is the chord, U is the freestream velocity, and C_l and C_d are the lift and drag coefficients determined from the airfoil lookup tables. Once these forces are determined at each location, they are modified to produce a fraction of the total force as given in the following equations

$$F_1 = \frac{F_z N_b}{N_\theta - 1} \quad \text{and} \quad F_2 = \frac{F_x N_b}{N_\theta - 1}, \tag{8}$$

where N_b is the number of blades, and N_θ is the number of azimuthal locations. The calculation in equation (8) is performed because for the actuator disc, the blade is assumed to be at each azimuthal location in an averaged sense that represents how often the blade will be present in that location over one revolution. These are the source terms that are applied at the appropriate grid points at each time step.

For the blade element model, Prandtl tip and hub-loss corrections described by Mikkelsen[30] were also implemented. Characteristic boundary conditions are used at all sides of the domain so that the modeled inflow is entirely uniform. Characteristic boundary conditions use Riemann invariants to automatically determine if a boundary has to be treated as inflow or outflow (this type of boundary condition is typically described as 'Opening' in commercial CFD solvers).

3.2.1. Computational setup.

FLOWYO utilizes an overset grid system for modeling the actuator disc and wake field. Typically, an actuator disc grid of cylindrical topology was embedded inside a stretched Cartesian grid. The FLOWYO code is fully parallel and was typically run on 128 processors. For both the RANS simulations and LES of the Phase VI rotor, a total grid size of (60 R × 20 R × 24 R) was used, where x is the flow direction, y is the horizontal, and z is the vertical direction. In the axial flow direction, there was 20 R spacing in front of the turbine and 40 R spacing downstream in order to convect the wake

Table I. FLOWYO grid independence study at $7m\ s^{-1}$.

Grid step	Off-body nodes	Near-body nodes	RANS power [W]	LES power [W]
NREL data			6042	6042
Refined	6.31×10^6	7.54×10^5	6214	6198
Step 1	4.66×10^6	5.72×10^5	6576	6558
Step 2	2.81×10^6	3.29×10^5	5946	6033
Step 3	1.07×10^6	1.18×10^5	5352	5387

for long distances. These dimensions will depend some on the flow velocity, scale of the turbine and desired distance to track the wake. The actuator disc grid (near-body) had 7.54×10^5 points and the off-body grid had 6.31×10^6 grid points. The grid points surrounding the location of the actuator disc loading points had a grid resolution of approximately 10 cm in the radial and axial directions. There were 109 points in the circumferential direction of the grid giving a resolution of approximately 30 cm at the tip and 5 cm at the root of the disc. The actuator disc grid in the near wake was also refined to prevent excessive numerical dissipation directly behind the turbine. The actuator disc grid had a radius of twice the rotor radius and an axial length of 16 R. Grid independence and power/wake convergence studies are performed for the RANS and LES in the following sections.

3.2.2. Grid independence study.

Several guidelines have been developed while testing various overset grids. The filter width, $\Delta = (\Delta x \Delta y \Delta z)^{1/3}$, was first varied between the near and off-body grids, and it was found that the ratio of the filter widths between the near and off-body should not exceed 4. Increasing the filter width ratio above 4 caused artificial turbulence production at the boundaries between the near-body and off-body grids. On the basis of this finding, the filter width was then held constant at near 3 and, the refinement level of the near-body and off-body grids were varied. Table I describes the four grids of varying refinement and the resulting power for the NREL turbine at $7m\ s^{-1}$ for both the RANS simulations and LES. The step 1, 2, and 3 grids scale down the number of nodes in the near and off body that were used while the filter width ratio is kept constant.

Considering the results in Table I, the step 1 and step 2 grids, which have 74% and 43% of the nodes in the refined grid, respectively, produce power results at less than 6% deviation from the refined grid for both RANS and LES. It was only for the step 3 grid, which includes 13% of the nodes in the refined mesh that a significant deviation in power of 14% from the refined grid occurs. It is hypothesized that coarsening the grid decreases the power because of the number of grid points along the radius of the blade. Although it was expected that the grid used for LES simulations would need to be more refined than the grid for the RANS cases, the deviation of power is similar for the RANS and LES cases as the grid is coarsened. The refined grid in Table I performed well for both the RANS simulations and LES.

To further test the dependability of the various grids, the wake velocities at 5 R, 10 R, 15 R, and 20 R were also compared using RANS. At each of the downstream locations, there was only a noticeable change in the wake velocity profiles when using the coarsest step 3 grid. This study indicates that numerical dissipation is not significantly affecting the RANS results at the turbine or in the wake.

3.2.3. Convergence study.

The convergence of power and the wind velocities were also studied for FLOWYO using RANS at $7m\ s^{-1}$. The RANS simulations were performed using the S–A turbulence model. Figure 4(a) shows the convergence of power using the refined grid, and Figure 4(b) shows the convergence of the velocities at 5 R, 10 R, 15 R, and 20 R for the refined grid. The power of the turbine converges after approximately 1×10^4 steps, which happens well before the wake velocities converge, even at 5 R in the wake. This demonstrates that power convergence can be obtained by only resolving the wake to very short distances downstream of the turbine. The wake velocities at 5 R, 10 R, 15 R, and 20 R take approximately $3.5 \times 10^4, 4 \times 10^4, 4.5 \times 10^4$, and 5×10^4 steps, respectively, to converge to within 1% of their final value. The wake velocities at each wake location converge to very similar values, which was not expected. This is a product of the actuator disc method and the S–A turbulence model, which is further discussed in the results.

3.3. *HELIOS* full rotor model

The flow patterns around a rotating wind turbine are dominated by vortex structures shed from the blades. Resolution of these wake structures requires low dissipation CFD algorithms and good grid resolution. Solution-based adaptive mesh refinement (AMR) is the most effective approach for maintaining good grid resolution and keeping the problem still tractable.[34]

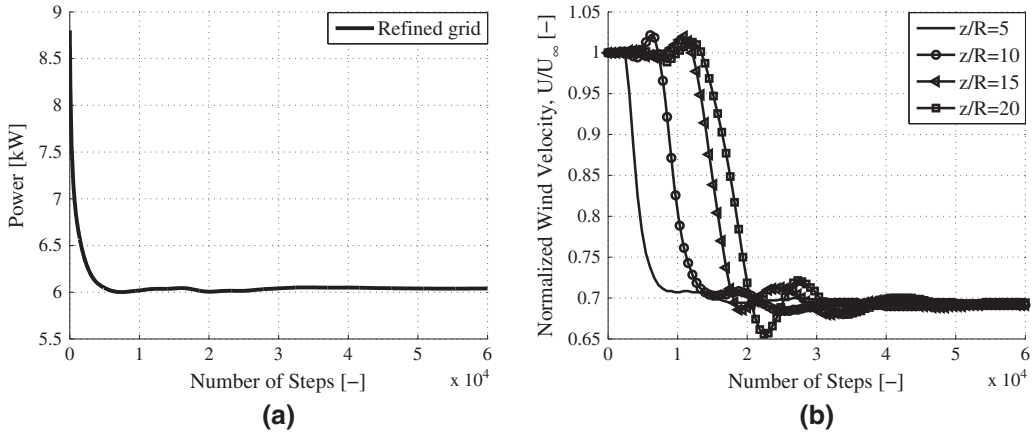

Figure 4. Convergence of (a) power for refined grid and (b) normalized wind velocities at a horizontal location of 0.5 R and axial locations of 5 R, 10 R, 15 R, and 20 R downstream of the turbine at $7m\,s^{-1}$.

Traditional CFD codes are often built on a single gridding paradigm namely structured curvilinear type, unstructured, or Cartesian. Structured curvilinear grids and unstructured grids are body conforming and provide good modeling capabilities for flow gradients/features near the no-slip boundaries. However, AMR is complex and often quite inefficient for these grid types. Cartesian grids on the other hand provide a simple and efficient way for performing AMR and are also very efficient for higher order low dissipation algorithms. Therefore, a good modeling approach for a wind turbine would be a hybrid overset grid approach that uses body-conforming grids close to the body and Cartesian grids with AMR away from the body. HELIOS[35] provides this state-of-the-art capability, and hence considerably improves the modeling of the turbine wakes. The following paragraph describes the main features of the numerical algorithms in the HELIOS code.

The near-body solvers utilized in HELIOS for this work are the NSU3D[11] and FLOWYO[18] codes developed at the University of Wyoming. NSU3D is a well-established finite volume-based flow solver for mixed element unstructured grids. It uses second-order discretization in space with implicit BDF2 in time. FLOWYO, which was previously described for the actuator disc simulations, is a multi-purpose solver that is capable of many different setups and numerical schemes. When used within the HELIOS framework, FLOWYO models the full rotor and solves RANS equations on a structured curvilinear mesh topology. A node-centered finite volume scheme is utilized, inviscid fluxes are discretized using a fifth-order weighted essentially nonoscillatory (WENO) upwind scheme, and viscous fluxes are discretized using a fourth-order central discretization. Roe's approximate Riemann solver is utilized to compute the interface inviscid fluxes. Implicit second-order backwards in time stepping along with Newton type non-linear sub-iterations are used to ensure time-accuracy at each physical step. For wind turbine calculations, low Mach preconditioning is applied to improve convergence and also to minimize the numerical dissipation introduced by the Riemann solver. The off-body solver SAMARC[36] is developed at the Army Aeroflightdynamics directorate. SAMARC uses a sixth-order accurate finite difference spatial discretization for the inviscid fluxes and explicit time integration using a three-stage Runge-Kutta scheme. Finally, the domain connectivity module PUNDIT[37] (also developed at the University of Wyoming) provides the overset grid assembling capability and facilitates data transfer between the near-body and off-body grid systems. All HELIOS simulations shown in this paper utilize the Spalart-Allmaras turbulence model,[28] which can be run in RANS or in DES mode[38] to achieve turbulence closure.

3.3.1. Computational setup.

An unstructured mixed element mesh with 3 million grid points is used for the near-body computations and extended to approximately one chord length from the wind turbine rotor surface. This grid encompasses both blades. There are approximately 70,000 nodes on the surface of the blade, which are clustered near the leading and trailing edge of the blades and also at the tip location. For each blade, there are approximately 175 points in the span-wise direction and 200 points along the airfoil contour. A no-slip boundary condition is utilized at the blade surface. The spacing normal to the wall has a $y+ = 1$ based on the chord Reynolds number. The outer boundaries of the near-body grid are overset with the off-body grid. Computations were performed using an off-body mesh system with solution AMR. The off-body mesh system consists of family of nested Cartesian grids with up to seven levels of refinement with each level twice as fine as its parent level. Characteristic boundary conditions are used at all sides of the domain so that the modeled inflow is entirely uniform.

For HELIOS simulations of the turbine performance, the wake was only convected to short distances downstream. Using AMR, the number of off-body nodes grew from 9 million to about 30 million in 20 adaptation cycles. About 5000 solution

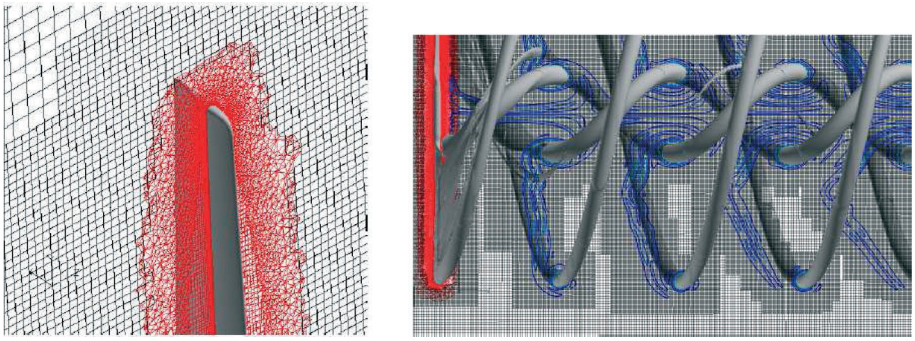

(a) Near-body mesh detail **(b)** Off-body mesh detail

Figure 5. HELIOS mesh system, illustrating overset grids for (a) near-body mesh and (b) off-body mesh with solution-based adaptive mesh refinement.

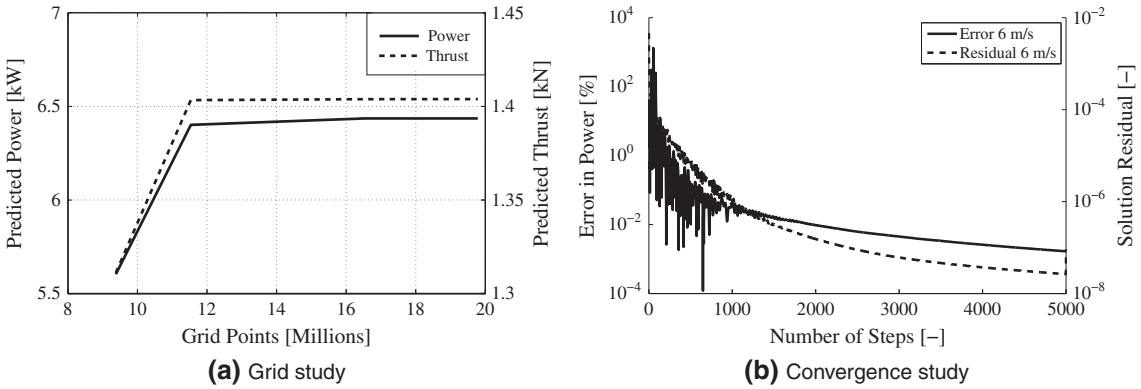

(a) Grid study **(b)** Convergence study

Figure 6. (a) HELIOS grid independence of power and thrust at $7m\ s^{-1}$ and (b) HELIOS power error and residual for at $6m\ s^{-1}$.

cycles were required to achieve power convergence. This required about 36 h on 64 Intel Xeon 2.67 GHz CPU processors. For the wake simulations back to 20 R, the off-body grid grew to around 160 million grid points. These simulations required the use of 512 processors and took approximately 1 week of simulation time. Using AMR, the mesh system efficiently tracks regions of high vorticity and provides sufficient grid resolution to maintain it un-dissipated for longer distances. This capability is critical for maintaining the tip and root vortices coherently for long distances. Traditional meshing approaches cause excessive numerical dissipation away from the turbine and tend to diffuse the vortex wake much faster than the physical diffusion rate. Therefore, the AMR capability is significant for obtaining accurate prediction of flow physics in the wind turbine wake. Figure 5(a) and (b) shows the mesh systems in HELIOS (both near body and off body with AMR).

3.3.2. Grid independence study.

HELIOS was tested with several different grids for the NREL Phase VI turbine in order to determine the grid size at which the power and thrust would converge. Figure 6(a) shows the grid convergence study at $7m\ s^{-1}$, both the thrust and power converge on a solution when slightly less than 12 million grid points are used.

3.3.3. Convergence study.

The power and thrust convergence of HELIOS were also considered in terms of power error and residuals. Figure 6(b) shows a plot of power error and residual for the NREL Phase VI turbine at $6m\ s^{-1}$ wind speed, plotted in a semi-log scale. The % error in power falls below 10^{-2}% after just 2000 solution steps. Furthermore, the solution residual shows monotonic convergence trends after the initial transients, decreasing by about four orders of magnitude in 5000 steps.

3.4. Turbulence models

For the RANS simulations with FLOWYO and HELIOS, the standard S–A turbulence model[28] was used for closure. LES performed with FLOWYO use the SGS Smagorinsky model.[29] HELIOS with DES was accomplished by using a modified form of the S–A model.[38] Studying past work from the literature that used the S–A model, it was unclear whether the standard S–A model was sufficient for far wake modeling, so the adopted approach was to compare various turbulence modeling techniques.

The technique used to model the turbulence is critical in achieving realistic results. The $k-\epsilon$ turbulence model has been the standard in RANS CFD wake calculations, but after extensive modifications, significant shortcomings still exist in comparison to LES techniques. It was not expected that the S–A model would provide more consistent results than the $k-\epsilon$ model. Instead, because the S–A model is arguably one of the most popular one-equation models used in research and industry CFD codes, a detailed analysis of its performance in predicting wake effects when compared with LES and DES is warranted. The comparison of the results from the S–A model with LES and DES will help contribute to the discussion concerning RANS CFD usage for wakes.

3.4.1. *Spalart-Allmaras* model.

For the standard S–A model, the one-equation for turbulent eddy-viscosity is given as

$$\begin{aligned}\frac{\partial\tilde{\nu}}{\partial t}+u_j\frac{\partial\tilde{\nu}}{\partial x_j}&=C_{b1}\left(1-f_{t2}\right)\tilde{S}\tilde{\nu}-\left[C_{w1}f_w-\frac{C_{b1}}{\kappa^2}f_{t2}\right]\left(\frac{\tilde{\nu}}{d}\right)^2\\&\quad+\frac{1}{\sigma}\left[\frac{\partial}{\partial x_j}\left(\left(\nu+\tilde{\nu}\right)\frac{\partial\tilde{\nu}}{\partial x_j}\right)+C_{b2}\frac{\partial\tilde{\nu}}{\partial x_i}\frac{\partial\tilde{\nu}}{\partial x_i}\right].\end{aligned}\tag{9}$$

The quantity $\tilde{\nu}$ is related to the eddy-viscosity by

$$\mu_t=\rho\tilde{\nu}\frac{\left(\frac{\tilde{\nu}}{\nu}\right)^3}{\left(\frac{\tilde{\nu}}{\nu}\right)^3+c_{\nu1}^3},\tag{10}$$

where ν is the molecular kinematic viscosity, and $c_{\nu1}=7.1$. The details of the model constants are not given here, but can be found in the original work by Spalart and Allmaras.[28] On the right-hand side of equation (9) are the production, destruction, and diffusion terms, respectively. Two important features of this turbulence model are that the production term is directly dependent on the vorticity and that the destruction term is dependent on the distance from the nearest wall. While this model has been used extensively in the performance prediction of fixed wing aircraft, helicopters, and wind turbines and has been used specifically for the NREL Phase VI turbine,[10] the authors are not aware of its use for wind turbine wakes.

In the use of this model for helicopters, it has been suggested that the standard model is not sufficient for capturing highly vortical flows, such as in the area of the wing tip vortex. Potsdam[39] noted that, in wall-bounded flows, the strain and vorticity are of similar magnitude, which makes the dependence of the production term on vorticity reasonable. In a vortex core, on the other hand, where the vorticity is high, but the strain is low, the eddy-viscosity can be largely over-predicted. Potsdam and other researchers have applied several rotational corrections[40] to account for this shortcoming. In the present study, the rotational correction was not applied in the FLOWYO or HELIOS simulations as it was desired to test the standard model.

For HELIOS simulations, a hybrid DES version of the S–A[38] was also utilized for predicting the downstream wake velocities. This version of the model treats near-wall regions in a RANS-like manner and treats the rest of the flow in an Smagorinsky-like manner. The change to the standard S–A model is made by modifying the distance parameter d in the original model with the distance function in the following equation:

$$\tilde{d}=min[d,C_{DES}\Delta],\tag{11}$$

where C_{DES} is a constant equal to 0.65, and Δ is the largest dimension of the grid cell.

3.4.2. Smagorinsky.

The Smagorinsky SGS model[29] was used in all LES calculations with FLOWYO. By using the Smagorinsky model, the eddy-viscosity is defined as

$$\nu_t=(C_s\Delta_g)^2\sqrt{2\bar{S}_{ij}\bar{S}_{ij}}=(C_s\Delta_g)^2|S|,\tag{12}$$

where Δ_g is the grid size, C_s is a constant with a value between 0.1 and 0.2 and $\bar{S}_{ij}$ is the rate-of-strain tensor.

3.5. Computational fluid dynamics/computational structural dynamics coupling for yawed inflow

Inflow conditions with yaw errors create an in-plane component in the velocity field encountered by wind turbines. This in-plane field creates a periodically changing aerodynamic setting for each of the turbine blades leading to a cyclic variation of both aerodynamic and structural dynamic loads. Turbine elasticity does play an important role under these conditions as cyclic variation of loading creates corresponding structural deformation patterns. Therefore, a methodology that includes fluid/structure coupling is explored for yawed flow cases with a multibody system dynamics (MSD) used for solving the structural dynamics. Fluid/structure interfaces are developed for both of the aerodynamic modeling approaches that allow modeling of discrete blades, that is, HELIOS and UWAKE. A brief description of both the multibody solver and the fluid/structure interface development is given here.

3.5.1. Multibody solver.

The proposed MSD analysis is based on MBDyn, a free general-purpose multibody solver developed at the Politecnico di Milano.[41–43]

It solves initial value problems (IVP) related to generic multiphysics models, biased toward rotary wing aeroelasticity. The structural analysis consists in writing Newton-Euler equations of motion of a set of rigid bodies,

$$\mathbf{M}(x)\dot{x} = q \tag{13a}$$

$$\dot{q} = f(x, \dot{x}, t), \tag{13b}$$

connected by deformable elements and kinematic constraints. The kinematic variables x include rotation parameters. The equations of motion consist in force and moment equilibrium of each body as functions of the momentum and momenta moment variables g.

Deformable elements, for example, geometrically exact, nonlinear finite element-like beams[44] are used for the structural modeling of the blades. Kinematic constraints, like those used to model the blade pitch mechanism and the rotation imposed to the hub, are explicitly added to the problem as algebraic relationships between the Cartesian coordinates x of the bodies, $\phi(x, t) = 0$. The constraints are enforced using Lagrange's multipliers $\boldsymbol{\lambda}$. The resulting differential-algebraic equations,

$$\mathbf{M}(x)\dot{x} = q \tag{14a}$$

$$\dot{q} + \phi_{/x}^{T}\boldsymbol{\lambda} = f(x, \dot{x}, t) \tag{14b}$$

$$\phi(x, t) = 0, \tag{14c}$$

are integrated in time using implicit multistep integration schemes.[45]

Arbitrary rotations are dealt with using an incremental approach. The orientation of each body at a given time step is described using its orientation $\mathbf{R}_k$. The incremental orientation between two time steps is $\mathbf{R}_{k-1,k}$, such that $\mathbf{R}_k = \mathbf{R}_{k-1}\mathbf{R}_{k-1,k}$. Since the problem is solved using a predictor-corrector scheme, the incremental orientation $\mathbf{R}_{k-1,k}$ is decomposed as $\mathbf{R}_{k-1,k} = \mathbf{R}^{(0)}\mathbf{R}_{\Delta}$, where $\mathbf{R}^{(0)}$ is the predicted increment of orientation, which remains constant during the subsequent correction phase of the numerical solution, whereas $\mathbf{R}_{\Delta}$ is unknown. The operator $\mathbf{R}_{\Delta}$ is described in terms of the Cayley-Gibbs-Rodrigues parameters,

$$\mathbf{R}_{\Delta} = \mathbf{I} + \frac{4}{4 + g \cdot g}\left(g\times + \frac{1}{2}g \times g\times\right), \tag{15}$$

a very efficient parametrization that does not use trigonometric operations.[46] As a consequence, the orientation increment is small with respect not only to the rotation that results in a singularity of the parametrization, π, but also to the order of the integration scheme, $\|g\| = o(\Delta t^n)$, thus allowing significant simplifications in the formulation of the Jacobian matrix of the problem.

The solver has been recently applied to wind turbine aeroelastic analysis, using blade element model aerodynamics using either the built-in formulation[41] or NREL's AeroDyn routines.[47] The fluid structure interface presented here is an extension of the methodology originally developed and presented by the authors.[48]

3.5.2. Fluid/structure interface.

The aerodynamic and MSD analyses are coupled using communication primitives provided by MBDyn. A generic external force element allows for communication of the kinematics of a set of finite element nodes, essentially the position and orientation contained in x and the corresponding linear and angular velocities contained in $\dot{x}$, to the peer analysis, the CFD in this case. The orientation of the nodes can be expressed in a choice of parametrizations, to ease their use in the

peer solver. The kinematics can be transmitted either in the absolute reference frame or in the relative frame of a reference node; in the latter case, the absolute kinematics of the reference node are transmitted as well.

In principle, the coupling can be performed at the iteration level, so that the two analyses simultaneously and cooperatively converge to a fully-coupled solution at each time step, as carried out for example in.[42] The MSD solver sends the predicted kinematics; based on that, the CFD solver computes the aerodynamic loads and sends them back to the MSD solver; the latter performs one iteration applying the aerodynamic loads received from the CFD, updates the kinematics and sends them back to the CFD solver. The process is repeated until the CFD solver considers the flow solution converged. From this point on, the MSD solver iterates keeping the aerodynamic loads constant until convergence. The process is repeated for the following time step.

Given the relatively short time step required for accuracy by the CFD analysis, corresponding to 0.25°, only one exchange is actually required for each time step, as the predicted kinematics result in smooth aerodynamic load changes that allow the structural solution to converge very quickly without appreciable correction to the kinematics.

4. RESULTS

The first objective is to validate the aerodynamic loads prediction of the three methods UWAKE, FLOWYO (RANS), and HELIOS (RANS) versus the NREL Phase VI experimental data. Calculations are performed on the NREL Phase VI rotor from 5–20 $m\ s^{-1}$ wind speeds. The NREL data are shown with +/- one standard deviation for all measurements, which indicate the variation over one revolution of the blade. For uniform axial inflow, the aerodynamic power, thrust and spanloads are compared for each of the CFD methodologies. The suction surface streamlines simulated by HELIOS are also provided. All of the methodologies are then used for computation of the wake of the NREL turbine to 20 R downstream, including a comparison of FLOWYO with RANS/LES. For yawed inflow, the power, root bending moments, and sectional aerodynamic loading are shown for UWAKE and HELIOS (RANS).

4.1. National Renewable Energy Laboratory Phase VI axial flow results

4.1.1. Power and thrust curves.

Power and thrust predictions are shown in Figure 7(a) and (b) along with the NREL experimental data. For the power curve predictions, each of the methods are within 5% of the experimental data and within the experimental error bars up to 9 $m\ s^{-1}$, but after this the results differ. After approximately 9 $m\ s^{-1}$, the NREL turbine enters the stall portion of the power curve, and there are larger errors with the free-vortex and actuator disc approaches. While the reduced performance of these methods is well known once stall is initiated due to their dependence on 2D airfoil data, recommendations from Breton *et al.*,[27] as well as the findings of Tangler[49] and Sørensen[4] are used to achieve more acceptable results, especially for the free-vortex method. They showed that stall delay was significant over the inboard 80% span of the blade, while at the tip, there was a reduction in lift. Therefore, the stall-delay model is applied over only the inboard portion of the blade, and it is also ensured that the drag increases along with the lift coefficient. While out of the scope of the current work,

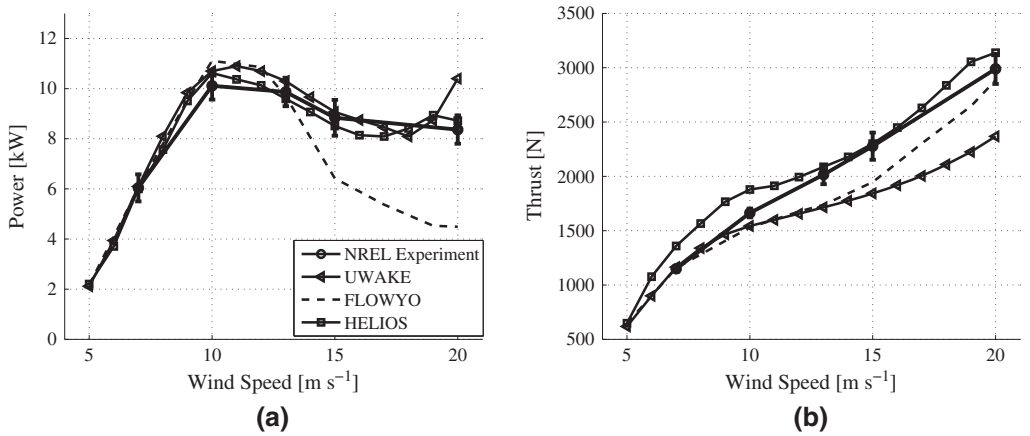

Figure 7. (a) Power and (b) thrust curve for UWAKE, FLOWYO (RANS), and HELIOS (RANS) versus National Renewable Energy Laboratory experimental data.

we concur with available literature that the development of correction methods be revisited. The thrust comparison of the UWAKE and FLOWYO codes with the NREL data also shows the same trends as the power.

HELIOS predictions prove the most accurate, especially in the stalled portion of the power curve. Power predictions with HELIOS are within the experimental error bars throughout the entire range of wind speeds, but there is a slight over-prediction of power at the initiation of stall. HELIOS does not include a transition model and instead models the flow over the blade as entirely turbulent. It is evident that including a transition model in HELIOS would further improve predictions near stall transition. The thrust is over-predicted by HELIOS between 6 and 10 $m\ s^{-1}$ but then falls very near the data at the higher wind speeds.

4.1.2. Spanload distributions and suction surface streamlines.

The spanload distributions of the normal force coefficient, Cn, and the tangential force coefficient, Ct, are then compared for each of the methods in relation to the NREL data. The normal coefficient and tangential coefficients at 7 $m\ s^{-1}$ can be seen in Figure 8(a) and (b), and the results at 10 $m\ s^{-1}$ are shown in Figure 9(a) and (b). The UWAKE and FLOWYO spanloads are first discussed, and then the HELIOS spanloads are described together with the surface streamlines.

Considering the Cn produced by FLOWYO and UWAKE at 7 $m\ s^{-1}$, good agreement between predictions and experimental data is shown, especially at the middle regions of the blade. It should be mentioned again that FLOWYO includes the Prandtl root and tip loss models[30] to compensate for the lack of distinct root and tip vortices generated by the actuator disc.

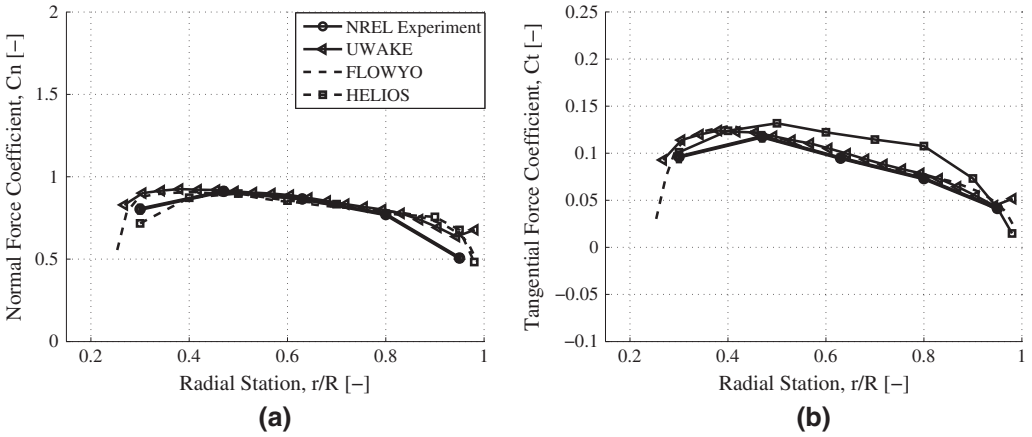

Figure 8. Spanload distributions of (a) normal force coefficient, Cn, and (b) tangential force coefficient, Ct, versus National Renewable Energy Laboratory experimental data at wind speed of 7 $m\ s^{-1}$.

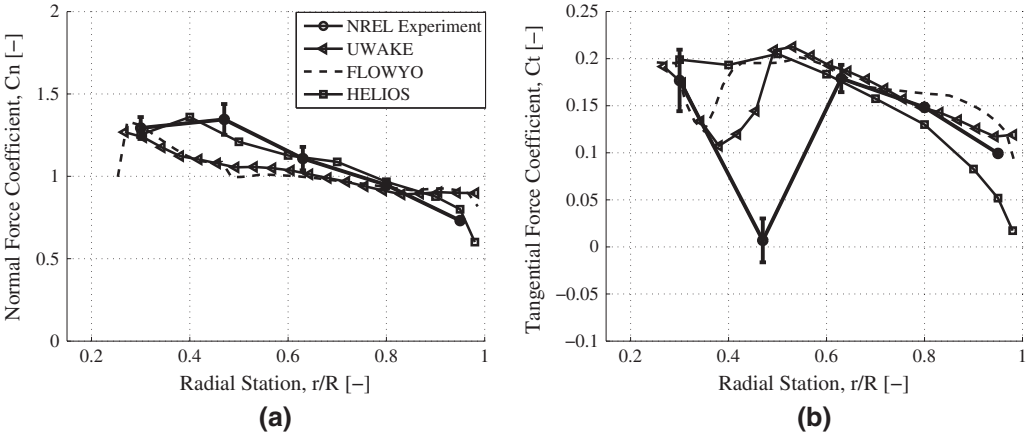

Figure 9. Spanload distributions of (a) normal force coefficient, Cn, and (b) tangential force coefficient, Ct, versus National Renewable Energy Laboratory experimental data at wind speed of 10 $m\ s^{-1}$.

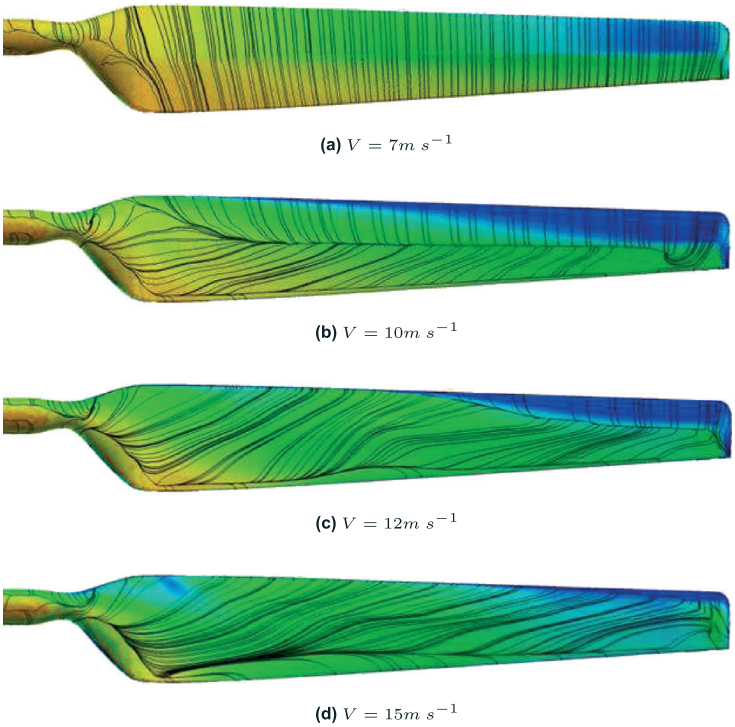

Figure 10. HELIOS suction surface streamlines for Phase VI blade at (a) 7, (b) 10, (c) 12, and (d) $15m\ s^{-1}$.

UWAKE on the other hand models the tip and root vortex, and the results near the tip are compatible between FLOWYO with the tip loss and UWAKE without. There is also close comparison of predicted and measured Ct for FLOWYO and UWAKE at 7 $m\ s^{-1}$.

Moving to the 10 $m\ s^{-1}$ cases, both UWAKE and FLOWYO significantly underpredict the inboard Cn at 10 $m\ s^{-1}$. This is the targeted region for the stall-delay model, which highlights the difficulty of accurately using this type of stall correction with blade element model prediction tools. There is a significant downturn in the experimental Cn near the 47% radial span location. This downturn is a result of the declining stall-delay outboard of this location. Tangler[49] explains that a decline of the delayed stall Cn in the spanwise direction leads to strong trailing vorticity near the 47% radial span. He also mentions that this trailing vorticity is the continuation of a standing, spanwise vortex, which lies on the suction surface. For the tangential force coefficient, UWAKE and FLOWYO with the stall-delay model actually show reasonable prediction of the stall delay near the root and also shows a large drop in Ct near the midspan, but the magnitude of the drop is not as severe as in the measurements. FLOWYO has difficulties near the tip region for both the Cn and the Ct, as both are overpredicted. The tip loss model in FLOWYO attempts to reproduce the dropoff in load that is produced by the tip vortex, but it appears that the application of the model may not extend far enough inboard as there is still overprediction of the loads in the $80-95\%$ span region.

HELIOS gives a more complete picture of the spanloads predictions as the numerical Cn and Ct spanloads can be viewed in combination with the surface streamlines as shown in Figure 10. HELIOS is able to very accurately capture the Cn at 7 and 10 $m\ s^{-1}$. The surface streamlines show that while at $7m\ s^{-1}$, the flow is attached over nearly the entire blade, there is significant separation occurring at 10 $m\ s^{-1}$. The Cn at the inboard region of the blade predicted by HELIOS at 10 $m\ s^{-1}$ is especially impressive compared with UWAKE and FLOWYO. HELIOS also slightly overpredicts the Ct curve at 7 $m\ s^{-1}$ and is not able to capture the large drop of Ct at the mid-span of the blade at 10 $m\ s^{-1}$. The streamlines at 10 $m\ s^{-1}$ show no evidence of the standing spanwise vortex. The overprediction of power for HELIOS at 10 $m\ s^{-1}$ is due to this difference in Ct at the mid-span, as the blade is more stalled than HELIOS is predicting. It is evident from the spanload results at 10 $m\ s^{-1}$ that while HELIOS does show some discrepancies with the experimental data, it is able to capture stall effects that are not successfully resolved by the other approaches. Including a transition model in HELIOS for future calculations should allow for improved prediction of both Cn and Ct at wind speeds near stall transition compared with the other models.

The predicted suction surface streamlines are also compared with those produced by the simulations of several other authors.[4,6,7,10] First, at 7 $m\ s^{-1}$, the extent of the root stall varies slightly, but in general, the results are quite consistent

between the each of the studies. The 10 $m\ s^{-1}$ streamlines present a very different story between the different approaches. Sørensen *et al.*[4] provided the closest predictions to measurements, and they explain that when 10 $m\ s^{-1}$ is reached, the separation point is abruptly moved to the leading edge near the 47% radial span location. It is also explained that at 10 $m\ s^{-1}$, the flow instabilities are large as massive stall is starting to occur. As the wind speed continues to increase to 12 $m\ s^{-1}$, HELIOS shows a leading edge separation point near the 63% span location and at 15 $m\ s^{-1}$ shows stall over most of the blade. Although not shown, the NREL Ct experimental data at 13 $m\ s^{-1}$ shows clear evidence of leading edge separation at the 63% span location, while the 80% station remains un-stalled. Then at 15 $m\ s^{-1}$, the data show leading edge stall extending to the 80% station. HELIOS appears to go from underpredicting the stall at 10 $m\ s^{-1}$ to slightly overpredicting the stall in the range of wind speeds from 12 to 15 $m\ s^{-1}$. HELIOS also slightly underpredicts the power in this range of wind speeds, which reflects the overprediction of stall. At even higher wind speeds, the stall area is spread over a larger portion of the blade and in general the modeling results agree more closely to each other and to measurements. The main area of discrepancy at higher wind speeds occurs in the area of the tip once the region has stalled.

4.1.3. Wake wind speed deficits.

Longer simulations were performed with each model to capture the downstream wind speed deficits back to 20 R in the wake at 5 and 10 $m\ s^{-1}$ wind speeds (the tip speed ratios, λ, are $\lambda = 7.59$ at 5 $m\ s^{-1}$ and $\lambda = 3.79$ at 10 $m\ s^{-1}$). These wind speeds are chosen mainly because of the large variation in thrust coefficient, which caused significant differences in the development and breakdown of the downstream wake. For each wind speed, the power and thrust coefficients are first given, and then the wake velocities and flow visualization are compared for each of the three CFD solvers.

The power coefficient, C_P, and thrust coefficient, C_T, predicted from each of the methods are shown in Table II. Also shown is the NREL experimental data at 10 $m\ s^{-1}$ plus or minus one standard deviation, which indicates the variation over one revolution of the blade. For both wind speeds, HELIOS predicts larger C_T values than the other two methods, which corresponds with larger wake deficits.

Figure 11 shows the comparisons of the wind speed deficits back to 20 R at a hub-height plane from each of the three methods. Each method produces a unique wind speed profile on the basis of the aerodynamic details that are captured at the turbine and the method for modeling the diffusion.

Figure 12 shows the wind speed deficits in the wake along a line from 3 R forward of the turbine to 20 R downstream of the turbine at a horizontal location of half the blade radius. Considering Figures 11 and 12 together, UWAKE predicts a maximum wind speed deficit of 67% of the freestream velocity at approximately 4 R downstream for the 5 $m\ s^{-1}$ case and a maximum deficit of 81% of the freestream wind speed at 7 R for the 10 $m\ s^{-1}$ case. The maximum deficit results compare favorably with 1D momentum theory, reaching approximately twice the induced velocity at the rotor. At 5 $m\ s^{-1}$, the average velocity at the rotor is 84% of the freestream, and at 10 $m\ s^{-1}$, the average induced velocity is 92% of the freestream. The decrease in velocity relative to the freestream for the 5 $m\ s^{-1}$ case is consistent with the larger C_T of 0.49, versus 0.34 for the 10 $m\ s^{-1}$ case. With a larger C_T, the wake deficits will be larger and the wake should break down at a faster rate, which is also consistent with the UWAKE results.

Once again comparing Figures 11 and 12, FLOWYO with LES predicts a maximum wind speed deficit of 70% of the freestream near 3 R for the 5 $m\ s^{-1}$ case and a maximum deficit of 83% of the freestream wind speed at 6 R for the 10 $m\ s^{-1}$ case. The maximum wind speed deficits are similar between FLOWYO and UWAKE, which is consistent with the closeness of the predicted turbine C_T for these models. There is very little diffusion of the wake when using RANS, whereas the wake profile is becoming more Gaussian like when using LES. The diffusion of the downstream wake is also similar between UWAKE and FLOWYO using LES. Specifically for the RANS simulations with FLOWYO, it does not appear that there is enough turbulent eddy-viscosity produced solely by the actuator disc to allow the wake to diffuse at similar levels to UWAKE or FLOWYO with LES.

This result begs the question of whether the actuator disc by itself is producing the appropriate vorticity levels and providing a good enough approximation for the structure of the wake. The actuator disc method lacks the distinct tip and

Table II. Power and thrust coefficients for National Renewable Energy Laboratory Phase VI turbine wake study.

Code/data	Wind speed [$m\ s^{-1}$]	C_P [-]	C_T [-]
UWAKE	5	0.33	0.49
FLOWYO	5	0.34	0.50
HELIOS	5	0.37	0.54
NREL data	10	0.21 ± 0.01	0.35 ± 0.01
UWAKE	10	0.22	0.34
FLOWYO	10	0.22	0.33
HELIOS	10	0.22	0.39

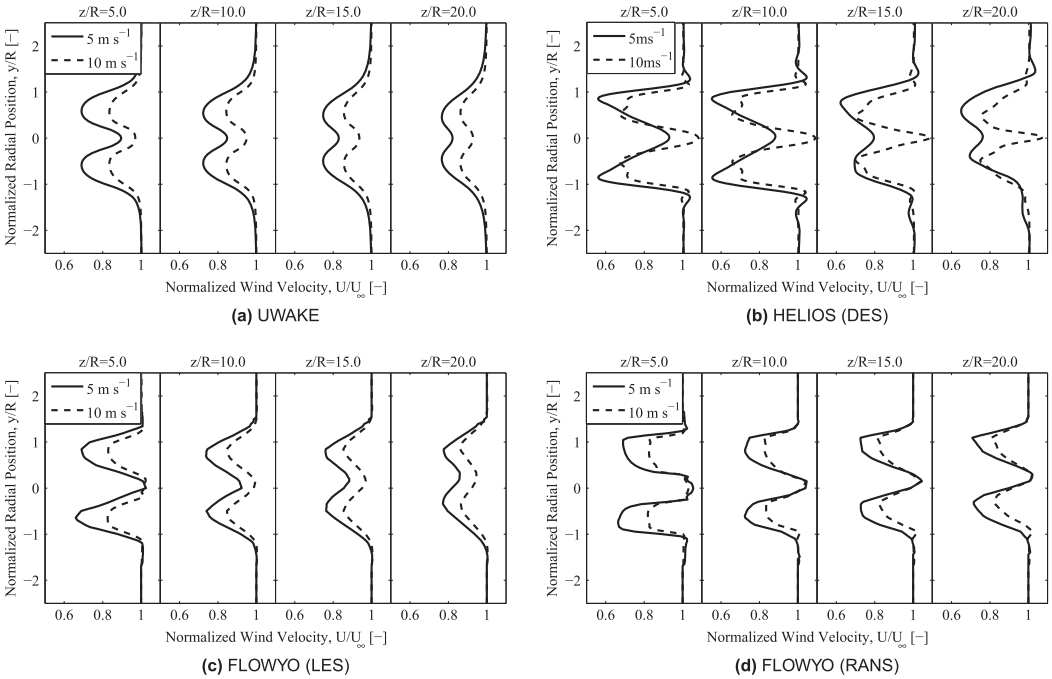

Figure 11. Normalized wind deficits at 5 and 10 $m\ s^{-1}$ for (a) UWAKE, (b) HELIOS (DES), and (c)–(d) FLOWYO (LES,RANS) at 5 R, 10 R, 15 R, and 20 R downstream of the turbine.

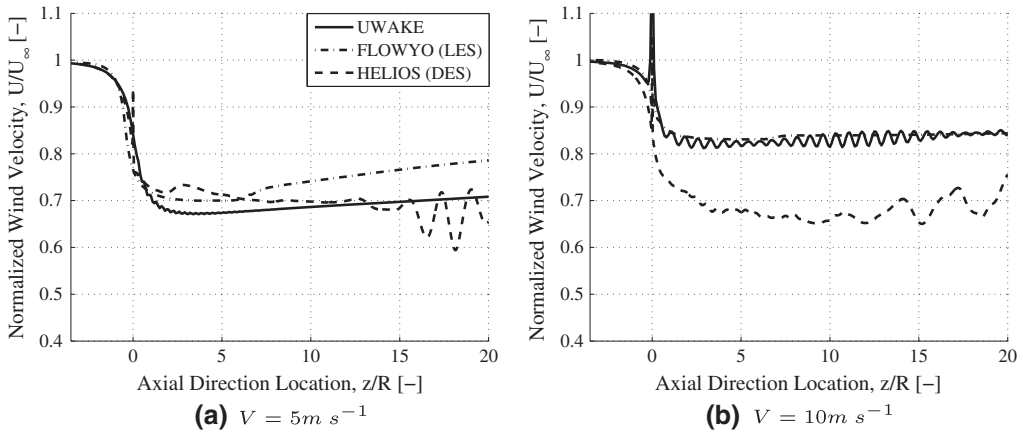

Figure 12. Normalized wind deficits along a line from 3 R forward to 20 R downstream of the turbine at a horizontal location of half the blade radius at (a) 5 and (b) 10 $m\ s^{-1}$ for each method.

root vortices and the maximum vorticity levels produced at the tip and root are approximately one-tenth of that produced in the full rotor simulations at 10 $m\ s^{-1}$. The main reason for the reduced vorticity at the tip and root is likely the coarser grid resolution in the actuator disc method compared with the full rotor method. The lack of diffusion for the FLOWYO RANS simulations compared with the LES is conjectured to be a result of the dependence of eddy-viscosity production on vorticity in the S–A turbulence model.

Finally, HELIOS with DES predicts a peak wind speed deficit of 58% of the freestream at 4 R downstream at 5 $m\ s^{-1}$ and 65% of the freestream at 9 R for the 10 $m\ s^{-1}$ case. The greater wind velocity deficits are consistent with the HELIOS C_T predictions that are larger than the other models. The modified DES version of the S–A model[38] is used in this simulation due to the issues found with using the standard S–A model with FLOWYO. The velocity and vorticity distributions in the wake produced by HELIOS create a more detailed description of the wake structure, as shown in Figure 13. Furthermore, in the HELIOS calculations, the more discrete and concentrated nature of the vortex structures cause the wake to destabilize

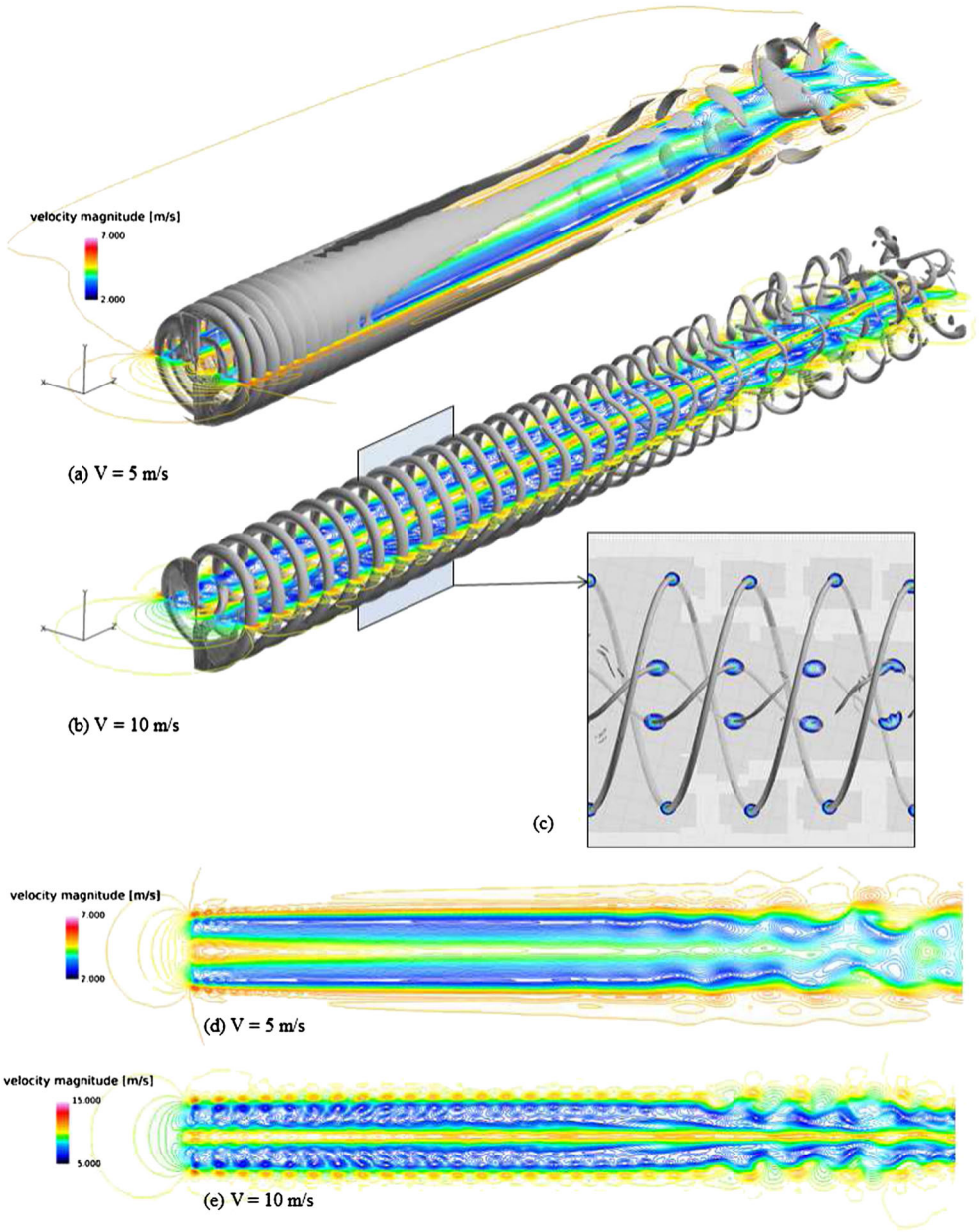

Figure 13. Visualization of the HELIOS wake. Top figures (a) and (b) show HELIOS vorticity iso-contours (w=3.0 s^{-1}) overlaid with velocity contours back to 20 R in the wake for the 5 and 10 $m\ s^{-1}$ solutions, respectively. The middle figure (c) shows how the adaptive meshing refines the grid surrounding the tip and root vortex. The tip and root vortices are shown with vorticity iso-surfaces (w=30 s^{-1}). Finally, horizontal slices of the wake velocity magnitude back to 20 R at 5 and 10 $m\ s^{-1}$ are shown in figures (d) and (e), respectively.

near 15 R downstream for the 5 $m\ s^{-1}$ case and near 20 R for the 10 $m\ s^{-1}$ case. The wake is observed to maintain a helical structure at 10 $m\ s^{-1}$, while at 5 $m\ s^{-1}$, the tip vortices merge and develop into a vortex tube.

4.2. National Renewable Energy Laboratory Phase VI yawed flow results

Yawed flow conditions (up to 60°) are simulated with full fluid structure coupling utilizing both of the aerodynamic prediction methods that allow modeling of discrete blades, namely HELIOS and UWAKE. In the results that follow, results

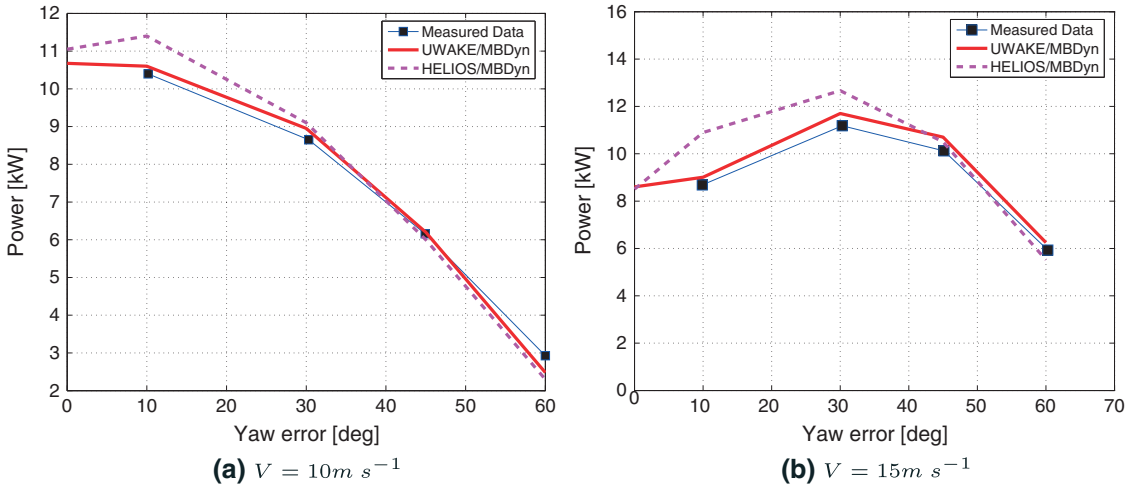

Figure 14. Power prediction based on low-speed shaft torque for different yaw error configurations.

using HELIOS and MBDyn coupling are denoted as HELIOS/MBDyn and results using UWAKE and MBDyn coupling are denoted as UWAKE/MBDyn. Structural dynamic and aerodynamic loading are plotted with fraction of rotor revolution as the x-axis coordinate. The starting reference for the rotor revolution (i.e., the zero azimuth coordinate) is when the blade is radially aligned with the tower and at its top most vertical location.

4.2.1. Power curves.

The wind turbine blade encounters a periodically changing aerodynamic setting at yawed inflow conditions. The resulting angle of attack can cause the blade sections to move in and out of stall regions. Therefore, it is possible that the power predictions reach a maximum at a non-zero yaw error conditions, especially at high wind speeds. Power results for yawed inflow at two representative wind speeds of 10 $m\ s^{-1}$ (stall onset) and 15 $m\ s^{-1}$ (post-stall) are presented here. Figure 14(a) shows the power variation at 10 $m\ s^{-1}$. Measured power reaches a maximum very close to zero yaw error at these conditions and continuously decreases as the yaw error increases. Both the analyses predict these trends quite accurately. UWAKE/MBDyn predictions have closer agreement with measured data at smaller yaw error angles. HELIOS/MBDyn predictions tends to over predict power at smaller yaw angles. At 15 $m\ s^{-1}$ (shown in Figure 14(b)), the maximum power is obtained at a yaw error of 30°. Again, the analyses and measurements show good qualitative agreement of the trends. UWAKE/MBDyn predictions appears to show close agreement with the measurement even in this case while HELIOS/MBDyn predictions show a similar overprediction trend as that observed at 10 $m\ s^{-1}$.

4.2.2. Root bending moments.

Figures 15 and 16 show the flapwise bending moment and edgewise moments at the root section of the blade at a yaw angle of 30°. The measured data waveform shows a low frequency (1/revolution) overlaid with a higher frequency (5/revolution). Both of the analyses show reasonable predictions of the mean bending moment and amplitude and phase of the low frequency variation (for both flap wise and edge wise moments and also at both wind speeds). The high frequency trends are completely unresolved in UWAKE/MBDyn analyses while HELIOS/MBDyn appears to capture small high frequency variations. As indicated by both Masarati[48] and Gupta,[12] even the estimated bending moment computed using measured aerodynamic loading does not capture the high-frequency variations in flap bending moments. There are several hypotheses for the origin of these high-frequency components, they are (a) blade structural mode excited by high frequency aerodynamic loading caused by cyclic stall patterns, (b) blade hub motion excited by tower modes, and (c) variations caused by gear-train mechanics. Of these, case (a) should be resolvable by the current analysis because full fluid/structure coupling is performed. However, uncertainties do exist in the blade structural properties,[48] which make matching the blade frequencies and mode shapes difficult. Case (b) was investigated in the same work[48] by including structural and aerodynamic models of the tower. However, no remarkable improvement could be obtained. Further refinement of structural property data and inclusion of multi-body dynamics to the gear-train mechanics are expected to show improvement in the predictions.

4.2.3. Sectional aerodynamic loading.

Integrated quantities such as flapwise and edgewise bending moments often mask the variations in actual aerodynamic loading. In Figures 17 and 18, the normal force and tangential force coefficients are shown for three span stations

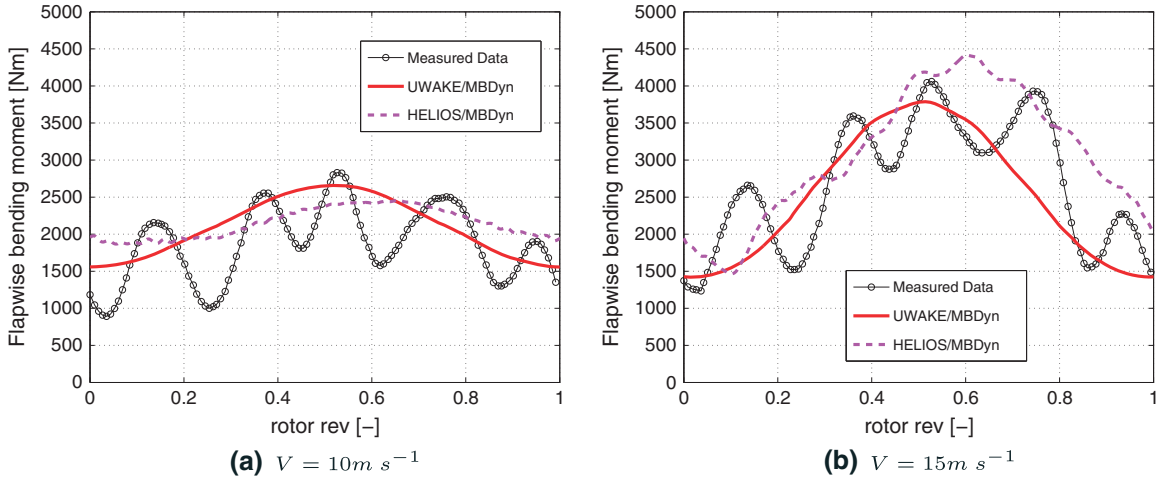

Figure 15. Flapwise bending moments at the root of the blade at 30° yaw error configuration.

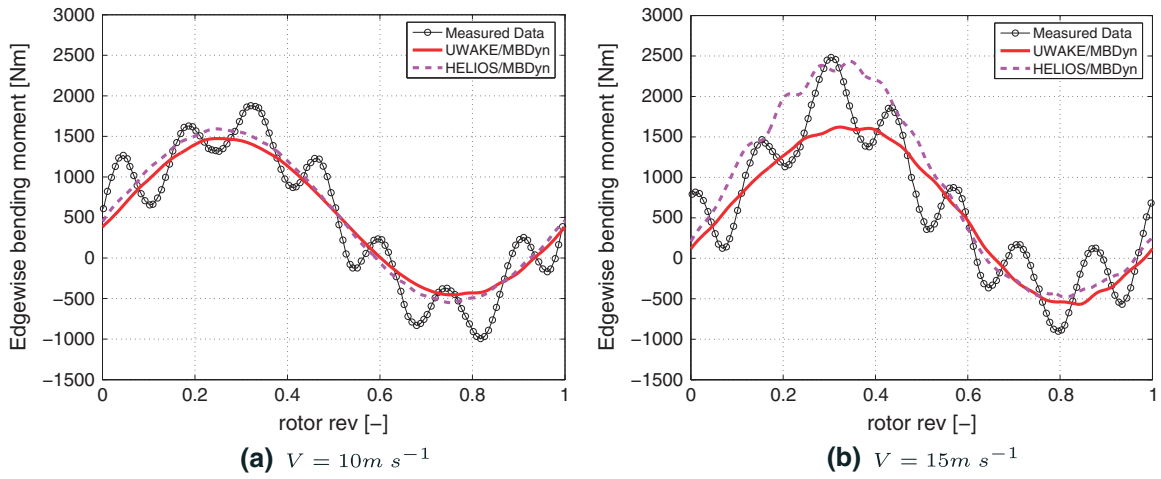

Figure 16. Edgewise bending moments at the root of the blade at 30° yaw error configuration.

at a yaw angle of 30°. Results for 10 $m\ s^{-1}$ are shown in the left column, and results for 15 $m\ s^{-1}$ are shown on the right column. In general, HELIOS/MBDyn predictions show closer agreement with the measurements. The asymmetric nature of the waveform is captured by the HELIOS/MBDyn analysis, while it remains largely unresolved in the UWAKE/MBDyn predictions. HELIOS/MBDyn results show large overpredictions at the beginning and ending phases of a rotor revolution, that is, at the high angle of attack regions and hence show larger mean values for both normal and tangential force coefficients. This observation is consistent with the over prediction of power noted before. UWAKE/MBDyn results show large disagreement with the nature of the waveform. However, there is good agreement in the prediction of the mean sectional force, which is also consistent with improved agreement in the power variation with measured data. The asymmetric nature of the waveform corresponding to the measured data is quite evident in all of the sectional aerodynamic loading plots. In Figures 19(a) and (b), where sectional normal and tangential force coefficients (at $r/R = 0.63, V = 15m\ s^{-1}, yaw = 30°$) are shown, we attempt to characterize the sources of this asymmetry. From the point of view of a blade section (at constant pitch setting), the variation of incident velocity field (excluding axial induction) is symmetric about 180° azimuth, that is, angle of incidence encountered at one-eighth of a rotor revolution will be exactly equal to that encountered at seven-eighths of a rotor revolution. Axial induction is weakly asymmetric because the vortex wake is closer to the plane of the turbine at one location compared to the other. Further, the asymmetry because of the vortex wake becomes weaker as one moves inboard. Dynamic stall is a second source of asymmetry, which causes asymmetric separation and reattachment and is quite sensitive to the three-dimensional nature of

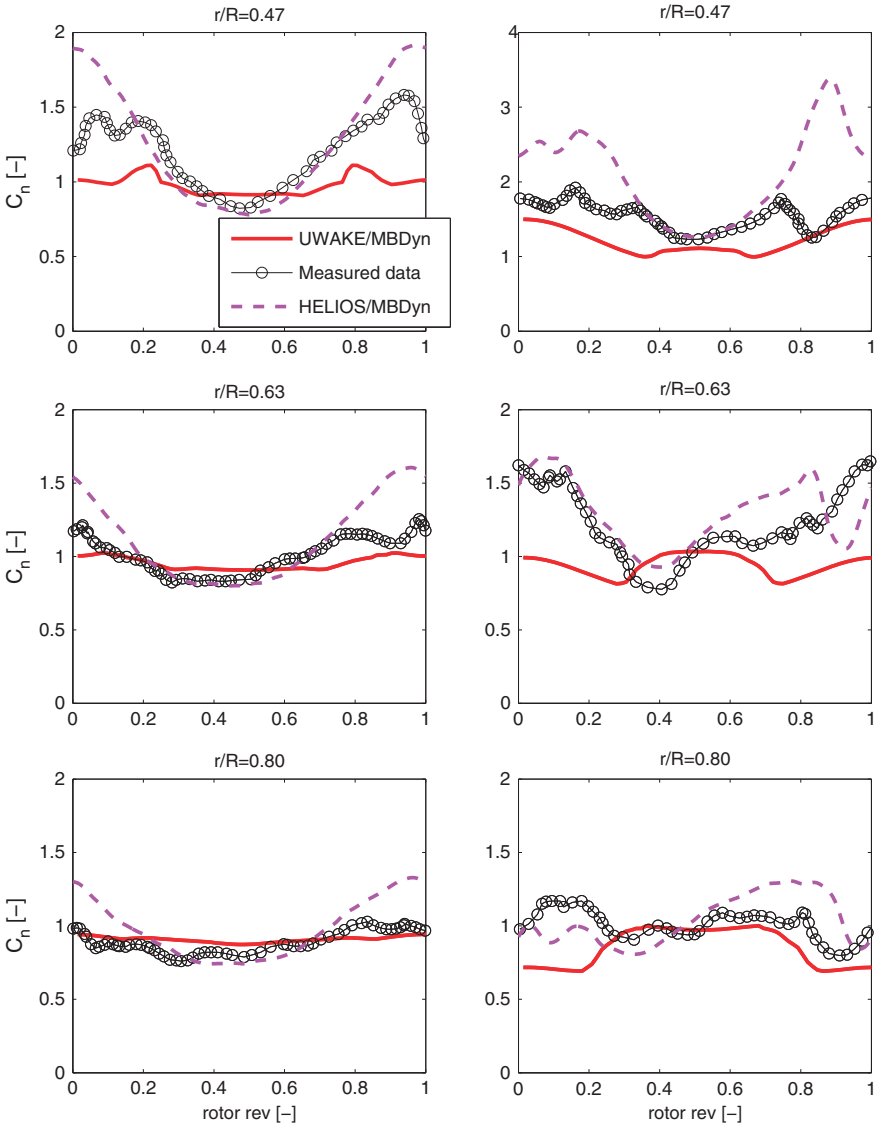

Figure 17. Sectional normal force coefficient for 30° yaw error condition where, left column : V=10 $m\ s^{-1}$, right column : V=15 $m\ s^{-1}$.

the flow field. Presence of radial flow is the main driver for three dimensional asymmetry. At regions where the blade rotation is toward the wind direction (termed as advancing side), the radial flow is directed from tip to root, while at regions where blade rotation is away from the wind direction (termed retreating side), the radial flow directed from root to tip.

The angle of attack obtained from the UWAKE analysis is shown in both Figures 19(a) and (b). Note that this angle of attack variation does include the effect of axial induction. It is apparent that the variation is quite symmetric. As a consequence, the aerodynamic coefficient variation computed by UWAKE is also symmetric—because UWAKE is a blade-element momentum-based method that uses sectional angle of attack as the basis for aerodynamic loading. Also note the strong stall patterns in the predicted aerodynamic loading corresponding to angle of attacks greater than 15°. Both measured data and HELIOS predictions show strongly asymmetric behavior. This shows the more complex three-dimensional nature of the flow field, that is, the presence of radial flow affects stall behavior. On the retreating side, significant stall characterized by loss of aerodynamic loading is observed (especially in HELIOS results), while on the advancing side aerodynamic loading tends to increase even in post-stall angle of attacks. The measured data shows similar trends, but the losses on the retreating side are not as dramatic as those produced by HELIOS.

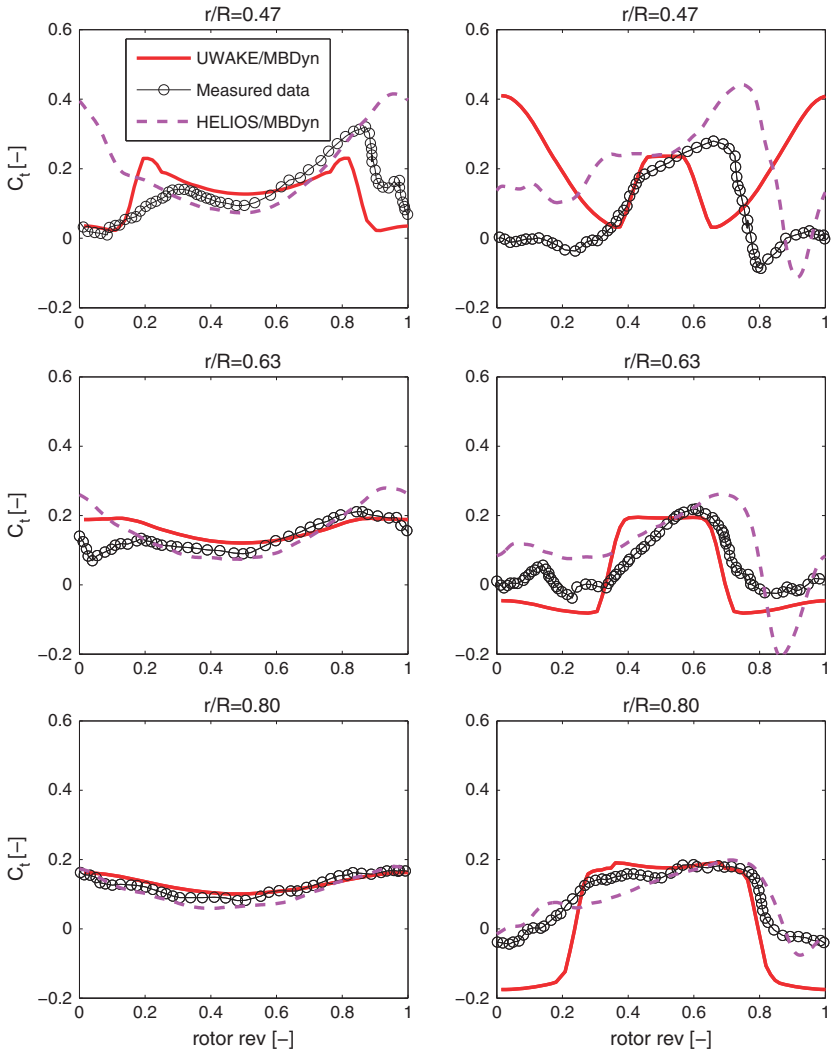

Figure 18. Sectional tangential force coefficient for 30° yaw error condition where, left column : V=10 $m\ s^{-1}$, right column : V=15 $m\ s^{-1}$.

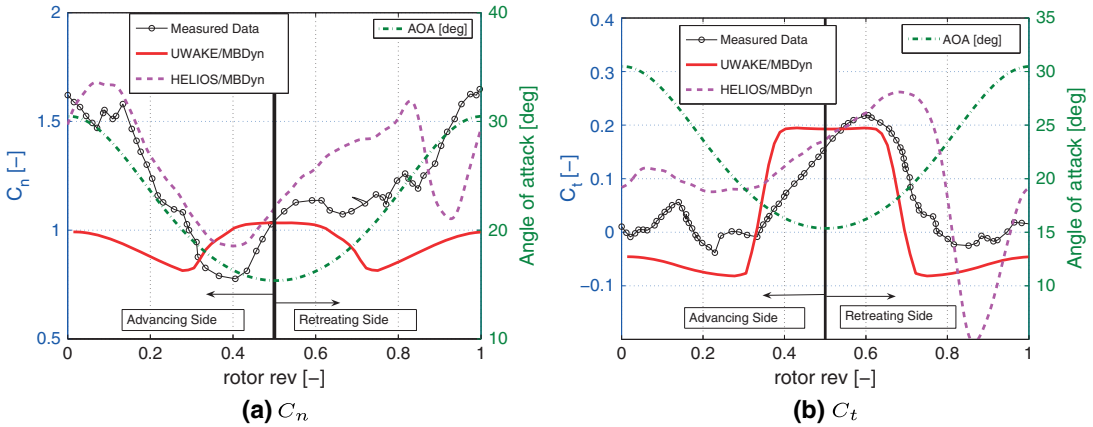

Figure 19. Sectional normal force coefficient, C_n, and tangential force coefficient, C_t, variations at $r/R = 0.63$ station for V=15 $m\ s^{-1}$ and yaw error of 30°.

5. CONCLUSIONS

A detailed performance assessment of the NREL Phase VI turbine was completed with three incrementally complex methodologies, namely UWAKE (free-vortex wake method), FLOWYO (actuator disc CFD), and HELIOS (full rotor CFD). It is observed that the performance at pre-stalled conditions can be predicted quite accurately using low-complexity blade element model type methods (UWAKE/FLOWYO), and it also encouraging to note that the higher complexity model still retains the same level of accuracy as blade element model codes. The transition regime is not well predicted by any methodology, but HELIOS shows excellent results once stall spreads along the blade at the higher wind speeds. The adaptive meshing technique in HELIOS proved to be beneficial for resolving the far wake but showed no remarkable benefits for the performance prediction, which required only the near wake (less than a radius length from the turbine) to be resolved. Three-dimensional effects shown in the post-stall results for HELIOS need to be further analyzed to develop correction schemes for the two-dimensional airfoil data that are utilized by the other methods. Studies of performance, aerodynamic, and structural dynamic loading under yawed flow condition led to two primary observations; (a) the free-vortex wake method (UWAKE) is as reliable as the full rotor method (HELIOS) in providing accurate prediction of integrated quantities (power and root bending moment) and (b) the full rotor method is more accurate in capturing detailed wave forms of sectional aerodynamic loading as it provides improved representation of the flow physics associated with radial flow and wake dynamics.

Studies of the wind turbine wakes in uniform inflow showed that the full rotor method produced the largest wind deficits and slowest dissipation rate for the far wake. The larger wind deficits predicted by HELIOS were consistent with a larger thrust coefficient at the turbine. The differences between each of the methods emphasizes the need of further detailed studies that can be augmented with experimental validation. The definition of the vortex core growth or viscous diffusion based on the vortex circulation in UWAKE performed adequately to produce a slowly developing Gaussian profile for the wake. An area of further work is to determine whether the core growth model can be appropriately modified when using turbulent inflow in conjunction with UWAKE. The computational times for this model are significantly faster that RANS, LES and DES and continuing to develop a physically reasonable viscous diffusion model could make this approach highly valuable for large scale wind farm studies using only limited computational resources. FLOWYO showed a different wake result between the RANS simulation and LES, with the LES producing a more realistically diffusing wake profile. Future studies will look at different levels of atmospheric turbulence and how it effects the diffusion of the wake with the actuator disc method.

For HELIOS, the strong and discrete vortex structures existed for up to 15 R in the wake and then destabilized. The downstream location of destabilization is observed to depend on the tip speed ratio and the thrust coefficient. It is worth noting that the AMR capability in HELIOS is the enabling technology for conducting tractable high resolution simulations demonstrated in this work. Without AMR and a coarser mesh system in the far wake, the numerical dissipation will overwhelm the physical diffusion rate and spread the wake at a much faster rate. On the other hand performing a simulation with a uniformly refined mesh system will required large amount of computational time and hence will become intractable. The present work clearly demonstrates the superior capabilities of the high resolution simulations in predicting the performance and resolving the details in the vortex wake, paving the way for future efforts to systematically analyze and understand the characteristics of the vortex wakes in wind farms.

ACKNOWLEDGEMENTS

The authors would like to acknowledge Dr. Bob Meakin who directs the DoD CREATE/AV program, as well as Dr. Roger Strawn and Mark Potsdam at the Army Aeroflightdynamics directorate at NASA Ames for providing access to the use of HELIOS software framework and the blade geometry for the NREL Phase VI turbine.

REFERENCES

1. Crespo A, Hernandez J, Frandsen S. Survey of modelling methods for wind turbine wakes and wind farms. *Wind Energy* 1999; **2**: 1–24.
2. Vermeer LJ, Sørensen JN, Crespo AS. Wind turbine wake aerodynamics. *Progress in Aerospace Science* 2003; **39**: 467–510.
3. Troldborg N. Actuator line modeling of wind turbine wakes, *Ph.D. Thesis*, Technical University of Denmark, 2008.
4. Sørensen NN, Michelsen JA, Schreck S. Navier-Stokes predictions of the NREL Phase VI rotor in the NASA Ames 80 ft x 120 ft wind tunnel. *Wind Energy* 2002; **5**: 151–169.
5. Johansen J, Sørensen NN, Michelsen JA. Detached-eddy simulation of flow around the NREL Phase VI blade. *Wind Energy* 2002; **5**: 185–197.

6. Duque EPN, Burklund MD, Johnson W. Navier-Stokes and comprehensive analysis performance predictions of the NREL Phase VI experiment. *Solar Energy Engineering* 2003; **125**: 457–467.
7. Zahle F, Sørensen NN, Johansen J. Wind turbine rotor-tower interaction using an incompressible overset grid method. *Wind Energy* 2009; **12**: 594–619.
8. LePape A, Lecanu J. 3D Navier-Stokes computations of a stall-regulated wind turbine. *Wind Energy* 2004; **7**: 309–324.
9. LePape A, Gleize V. Improved Navier-Stokes computations of a stall-regulated wind turbine using low Mach number preconditioning. *AIAA-2006-1502*, 2006.
10. Potsdam M, Mavriplis D. Unstructured mesh CFD aerodynamic analysis of the NREL Phase VI rotor. *AIAA-2009-1221*, 2009.
11. Mavriplis D. Grid resolution study of a drag prediction workshop configuration using the NSU3D unstructured mesh solver. *AIAA-2005-4729*, 2005.
12. Gupta S, Leishman JG. Performance predictions of the NREL Phase VI combined experiment rotor using a free-vortex wake model. *AIAA-2006-390*, 2006.
13. Sant T, van Kuik G, van Bussel GJW. Estimating the angle of attack from blade pressure measurements on the NREL Phase VI rotor using a free wake vortex model: axial conditions. *Wind Energy* 2006; **9**: 549–577.
14. Schmitz S, Chattot JJ. Characterization of three-dimensional effects for the rotating and parked NREL Phase VI wind turbine. *ASME Journal of Solar Energy Engineering* 2006; **128**: 445–454.
15. Hand MM, Simms DA, Fingersh LJ, Jager DW, Cotrell JR, Schreck SJ, Larwood SM, Unsteady aerodynamics experiment Phase VI: wind tunnel test configurations and available data campaigns. *Nrel/tp-500-29955*, NREL, Golden, CO, 2001.
16. Simms DA, Schreck SJ, Hand MM, Fingersh LJ, NREL unsteady aerodynamics experiment in the NASA Ames wind tunnel: a comparison of predictions to measurements. *Nrel/tp-500-29494*, NREL, Golden, CO, 2001.
17. Schreck SJ. The NREL full-scale wind tunnel experiment introduction to the special issue. *Wind Energy* 2002; **5**: 77–84.
18. Gundling C. Development and application of incrementally complex tools for wind turbine aerodynamics, *Ph.D. Thesis*, 2013.
19. Bhagwat M, Leishman JG. Stability, consistency and convergence of time-marching free-vortex rotor wake algorithms. *Journal of American Helicopter Society* 2001; **46**: 59–71.
20. Ananthan S, Leishman JG, Ramasamy M. The role of filament stretching in the free-vortex modeling of rotor wakes. *American Helicopter Society 58th Annual National Forum* 2002.
21. Gupta S. Development of a time-accurate viscous Lagrangian vortex wake model for wind turbine applications, *Ph.D. Thesis*, 2006.
22. Squire HB. The growth of a vortex in turbulent flow. *Aeronautical Quarterly* 1965; **16**: 302–306.
23. Ramasamy M. Contributions to the measurement and analysis of helicopter blade tip vortices, *Ph.D. Thesis*, 2004.
24. Leishman JG. *Principles of helicopter aerodynamics* 2nd ed. Cambridge University Press: New York, 2006,735–744.
25. Du Z, Selig MS. A 3-D stall-delay model for horizontal axis wind turbine performance prediction. *AIAA-98-0021*, 1998.
26. Ruess RR. Effects of grit roughness and pitch oscillations on the S809 airfoil. *Nrel/tp-442-7817*, NREL, Golden, CO, 1995.
27. Breton SP, Coton F, Moe G. A study on rotational effects and different stall delay models using a prescribed wake vortex scheme and NREL Phase VI experiment data. *Wind Energy* 2008; **11**: 459–482.
28. Spalart PR, Allmaras SR. A one-equation turbulence model for aerodynamic flows. *La Recherche Aérospatiale* 1994; **1**: 5–12.
29. Smagorinsky J. General circulation experiments with the primitive equations. *Monthly Weather Review* 1963; **91**(3): 99–164.
30. Mikkelsen R. Actuator disc methods applied to wind turbines, *Ph.D. Thesis*, 2003.
31. Cabezón D, Migoya E, Crespo A. Comparison of turbulence models for the computational fluid dynamics simulation of wind turbine wakes in the atmospheric boundary layer. *Wind Energy* 2011; **14**: 909–921.
32. Réthoré P-E. Wind turbine wake in atmospheric turbulence, *Ph.D. Thesis*, 2009.
33. Stovall T, Pawlas G, Moriarty P. Wind farm wake simulations in OpenFOAM. *AIAA-2010-825*, 2010.
34. Kamkar SJ, Wissink AM, Sankaran V, Jameson A. Feature-driven Cartesian adaptive mesh refinement for vortex-dominated flows. *Journal of computational physics* 2011; **230**(16): 6271–6298.

35. Sankaran V, Sitaraman J, Wissink A, Sankaran V, Jayaraman B, Datta A, Yang Z, Mavriplis D, Saberi H, Potsdam M, O'Brien D, Cheng R, Hariharan N, Strawn R. Application of the HELIOS computational platform to rotorcraft flow fields. *AIAA-2010-1230*, 2010.
36. Wissink A, Sitaraman J, Mavriplis D, Pulliam T, Sankaran V. A Python-based infrastructure for overset CFD with adaptive Cartesian grids. *AIAA-2008-0927*, 2008.
37. Sitaraman J, Floros M, Wissink A, Potsdam M. Parallel unsteady overset mesh methodology for a multi-solver paradigm with adaptive Cartesian grids. *AIAA-2008-7177*, 2008.
38. Spalart PR, Jou WH, Stretlets M, Allmaras SR. Comments on the feasibility of LES for wings and on the hybrid RANS/LES approach. *Advances in DNS/LES, Proceedings of the First AFOSR International Conference on DNS/LES*, 1997.
39. Potsdam M, Pulliam T. Turbulence modeling treatment for rotocraft wakes. *AHS Aeromechanics Specialists Conference*, San Francisco, CA, 2008.
40. Dacles-Mariani J, Zilliac GG, Chow JS, Bradshaw P. Numerical/experimental study of a wingtip vortex in the near field. *AIAA Journal* 1995; **33**: 1561–1568.
41. Cavagna L, Fumagalli A, Masarati P, Morandini M, Mantegazza P. Real-time aeroservoelastic analysis of wind turbines by free multibody software. *Multibody Dynamics: Computational Methods and Applications*, 2011.
42. Cavagna L, Masarati P, Quaranta G. Simulation of maneuvering flexible aircraft by coupled multibody/CFD. *Multibody Dynamics 2009*, 2009.
43. Masarati P. MBDyn theory and developers manual version 1.X. *Dipartimento Di Ingegneria Aerospaziale, Politecnico Di Milano*, 2013.
44. Ghiringhelli GL, Masarati P, Mantegazza P. A multi-body implementation of finite volume beams. *AIAAJ* 2000; **38**(1): 131–138.
45. Masarati P, Lanz M, Mantegazza P. Multistep integration of ordinary, stiff and differential-algebraic problems for multibody dynamics applications. *Xvi Congresso Nazionale AIDAA*, Palermo, September 24–28, 2001; 71.1–10.
46. Bauchau OA, Trainelli L. The vectorial parameterization of rotation. *Nonlinear Dynamics* 2000; **32**(1): 71–92.
47. Meng F, Masarati P, van Tooren M. Free/open source multibody and aerodynamics software for aeroelastic analysis of wind turbines. *AIAA-2009-1040*, 2009.
48. Masarati P, Sitaraman J. Coupled CFD/multibody analysis of NREL unsteady aerodynamic experiment Phase VI rotor. *AIAA-2011-153*, 2011.
49. Tangler JL. Insight into wind turbine stall and post-stall aerodynamics. *Wind Energy* 2004; **7**: 247–260.